MATERIALS SCIENCE

Ultrathin crystalline silicon–based omnidirectional strain gauges for implantable/wearable characterization of soft tissue biomechanics

Bofan Hu[1,2]†, Dian Xu[3]†, Yuting Shao[1,4]†, Zhongyi Nie[5]†, Pengchuan Liu[1,2,6], Jinbao Li[3], Lianjie Zhou[1,2,6], Pei Wang[7], Ningge Huang[1,2,6], Junhan Liu[1,2,6], Yifei Lu[1,2,6], Zhongyuan Wu[1,2,6], Bo Wang[3], Yongfeng Mei[1,2,6]*, Mengdi Han[5]*, Rui Li[3]*, Enming Song[1,2,8]*

Monitoring soft-tissue biomechanics is of interest in biomedical research and clinical treatment of diseases. An important focus is biointegrated strain gauges that track time-dependent mechanics of targeted tissues with deforming surfaces over multidirections. Existing methods provide limited gauge factors, tailored for sensing within specific directions under quasi-static conditions. We present development and applicability of implantable/wearable strain gauges that integrate multiple ultrathin monocrystalline silicon–based sensors aligned with different directions, in stretchable formats for dynamically monitoring direction angle–sensitive strain. We experimentally and computationally establish operational principles, with theoretical systems that enable determination of intensities and direction of applied strains at an omnidirectional scale. Wearable evaluations range from cardiac pulse to intraocular pressure monitoring of eyeballs. The device can evaluate cardiac disorders of myocardial infarction and hypoxia of living rats and locate the pathological orientation associated with infarction, in designs with possibilities as biodegradable implants for stable operation. These findings create clinical significance of the devices for monitoring complex dynamic biomechanics.

INTRODUCTION

Advanced technologies for real-time, in vivo measurements of soft tissue biomechanics, at wide ranges of spatial scales that range from cellular resolution level to large-area organ systems (i.e., heart, skin, etc.), are of increasing importance in biomedical research and clinical therapy (*1*–*5*). A critical challenge is in the development of implantable/wearable electromechanical systems that enable continuous monitoring of mechanical properties of living tissues with deforming surfaces to track highly dynamic biomechanics that yield diagnostics associated with different pathophysiological conditions (*6*–*9*). Relevant examples include the characterization of epicardial mechanics related to arrhythmogenic activity at a specific direction/region of the heart, crucial to precise assessments of atrial fibrillation or ventricular tachycardia (*10*, *11*). Additional possibilities are in tracking cornea for intraocular pressure (IOP) of relevance to glaucoma and in strain mapping of facial expression, each of which involves miniaturized electromechanical devices interfacing with deformable tissue surfaces (*12*, *13*). In these cases, of particular interest is the clinical and experimental characterization of time-dependent biomechanics of targeted tissues for multi- and/or omnidirectional-scale detection, at sufficient measurement resolutions and frequencies compatible well with physiological activities.

Emerging systems of human-machine interfaces for physiological assessments offer powerful options, such as measuring electrocardiography and surface electromyography signals (*14*–*17*). These techniques involve large electrodes with limited signal-to-noise ratios and scalability. Hence, measurements on curved regions such as epicardial apex areas would lead to large uncertainty for operations. A key feature in this context is the design of a device platform that can bend, stretch, and twist while in contact with soft, moving tissues to minimize mechanical mismatch at the biotic/abiotic interface and to support stable operation. Recent research establishes the use of flexible strain gauges for the characterization of soft biomechanics, by measuring tiny biological deformations (*18*–*20*). Constituent material options range from organic films to nanomesh/particles and two-dimensional materials such as graphene, as demonstrated for monitoring human activities or facial expression recognition (*21*–*23*). Although promising, persistent challenges for these approaches remain in measurement capabilities that typically suffer from device-to-device variation.

Alternatives such as metal strain gauges provide some advantages, including high reliability, low flexural rigidity, and rapid response time under dynamic conditions but with limited gauge factor (GF; defined as the change of electrical resistance along the direction of geometrical change) (*24*). As a comparison, well-established inorganic semiconductor–based strain gauges can present superior levels of device functionality, with intrinsic GF (~100) that surpass that of metal sensors (~2) by orders of magnitude (*25*). Examples of monocrystalline silicon–based strain gauges offer exceptional characteristics, as designed for continuous strain monitoring of the heart, skin, and other organs, respectively. In many cases, however, these methods focus on sensing only within a defined direction and

[1]Shanghai Frontiers Science Research Base of Intelligent Optoelectronics and Perception, Institute of Optoelectronics, Department of Materials Science, Fudan University, Shanghai, China. [2]International Institute for Intelligent Nanorobots and Nanosystems, Fudan University, Shanghai 200438, China. [3]School of Mechanics and Aerospace Engineering, State Key Laboratory of Structural Analysis, Optimization and CAE Software for Industrial Equipment, and International Research Center for Computational Mechanics, Dalian University of Technology, Dalian 116024, China. [4]Department of Ophthalmology, Tongji Hospital, School of Medicine, Tongji University, Shanghai 200065, China. [5]Department of Biomedical Engineering, College of Future technology, Peking University, Beijing 100871, China. [6]Yiwu Research Institute of Fudan University, Yiwu, Zhejiang 322000, China. [7]Department of Cardiothoracic Surgery, The Second Affiliated Hospital of Naval Medical University (Second Military Medical University), Shanghai 200003, China. [8]State Key Laboratory of Integrated Chips and Systems, Frontier Institute of Chip and System, Fudan University, Shanghai 200438, China.
*Corresponding author. Email: yfm@fudan.edu.cn (Y.M.); hmd@pku.edu.cn (M.H.); ruili@dlut.edu.cn (R.L.); sem@fudan.edu.cn (E.S.)
†These authors contributed equally to this work.

lack the ability to determine multidirectional scale, thus limiting their applications for dynamically monitoring biomechanics such as identifying/locating complex cardiac diseases that arise from various directions/sites across the heart, such as arrhythmias and myocardial infarction (MI).

Here, this work reports a miniature strain gauge device for omnidirectionally tracking strain distribution, capable of high-precision measurements across tissue surfaces for stable operation. The platform incorporates four ultrathin monocrystalline silicon nanoribbons (Si-NRs) aligned to different directions for omnidirectionality in an octopus-like shape, as designed in stretchable sensors that can intimately contact with targeted soft tissues for strain monitoring with direction angle–sensitive responses. Experimental and simulation studies enable quantitative measurements of strain distribution for a wide range of strain, with various intensities and direction angles. A 45° angular coordinate system can be established to determine the intensity and direction angle for a randomized applied strain application using the omnidirectional strain sensors, with a deviation of ~1° for direction identification and high precision for intensity detection. Integration with biodegradable encapsulation materials enables these devices to be fully dissolvable implants for in vivo operation, with biocompatibility verified through cellular experiments. Examples of wearable evaluations range from facial expressions and cardiac pulse for human individuals to IOP assessments of porcine eyes. In vivo measurements on rat hearts validate the capabilities of disorder diagnosis such as arrhythmias and MI and accurately locate the infarct orientation related to the pathologies. These results create future opportunities for clinic use of continuous monitoring of tissue biomechanics and hospital diagnostics of related disorders and pathologies, especially for patients after cardiac surgeries.

RESULTS

Materials, structural design, integration schemes, and device characteristics

Figure 1A begins with the schematic illustration and optical image of the device, which we refer to as the omnidirectional strain gauge (OSG) device, serving as a wearable and implantable platform for mechanophysiological monitoring, in a biocompatible manner that can seamlessly mount on time-dynamic organs such as the skin or heart. The overall system consists of the four separate serpentine-shaped Si-NR–based sensors, as an octopus-like shape, uniformly aligned within an omnidirectional scale across tissue surface, each with a length of 3 mm and a width of 100 μm, at different orientations (labeled as S1 to S4) with an interval of 45°. Fabrication began with solid-state boron doping (960°C for 15 min) of p-type device Si on a Si on insulator (SOI; SOITEC) wafer with a doping concentration of ~10^{20} atoms/cm^3, followed by transfer printing onto a polyimide (PI) film on a temporary glass substrate. Sequences of lithographic patterning, etching, and integration with gold (200 nm thick) wire connection, embedded above and below by layers of PI (1.5 μm thick), yield serpentine electrical traces as resistive strain gauges in a stretchable format. Following the release of the device from the temporary substrate and application onto targeted biological tissues enables the wearable and implantable platform for biomechanical sensing. Information about device dimensions with layer thickness appears in Fig. 1A, and detailed fabrication processing can be found in fig. S1 and Materials and Methods.

Here, the overall device design provides an open mesh structure for a stable mechanical interface to enable efficient delivery of force between strain gauge and tissues. The right inset of Fig. 1A shows a measured example of cardiac monitoring with real-time signals of $\Delta R/R_0$ (ΔR corresponds to the relative change in electrical resistance of a representative Si-NR–based sensor; R_0 corresponds to the initial electrical resistance of the sensor). The total thickness of the OSG device is less than 4 μm; therefore, the resulting platform in ultrathin film form can directly couple to the complex surface of the skin or other organs by virtue of the water-soluble tape (WST; 3 M 5414 transparent) and commercial bioglue (Derma-tac, Smooth-On Inc.) for a conformal contact. Figure 1B shows the application of the OSG device on the wrist of a volunteer individual for monitoring the pulse signal, where the platform can interface seamlessly with the skin for subsequent long-term measurement. Figure S2 illustrates the associated attaching procedure of the device.

The adhesion interface between the device and targeted tissues such as the skin is of critical importance. Peel tests can enable the assessment of the device's adhesion under various conditions, including dry and sweaty states (fig. S3A; details are available in Materials and Methods). Figure S3 (B and C) presents the applied forces as a function of displacement in millimeters and yields comparable adhesion energies of 567.1 J/m^2 for the dry skin and 480.8 J/m^2 for the sweaty skin, respectively, indicating stable mechanical interfaces under different states (*26*, *27*).

Although useful in many cases, the approaches of lamination via WST might induce device failure and performance degradation when removed from the skin due to irreversible damage. To avoid these issues, OSG device reusability can be improved by introducing a thin layer of soft elastomer [polydimethylsiloxane (PDMS), 30 μm thick, with an elastic modulus of 500 kPa], as shown in fig. S4A. Details can be found in Materials and Methods. Hence, the OSG devices can mount on tissues intimately for multiple uses in a simple, reversible manner, where fig. S4B demonstrates that the reusable OSG device maintains stable electrical resistance and GF after 100 times of adhesion. However, the use of WST and bioadhesive glue enhances mechanical coupling at the interface between the device and tissues, facilitating the better transmission of skin strain to the device and thus resulting in higher GF than those onto PDMS substrate, indicating higher sensitivity, as indicated in fig. S4C (*18*, *28*), however, failing in multiple times of use.

For the performance characteristics, the OSG device is laminated onto a thin elastomer (PDMS, 1 mm thick, with moduli of 500 kPa) as the artificial skin substrate. Figure 1C shows the correlation between the electrical resistance response of a representative strain sensor of the OSG device and the applied strain along a fixed direction (intensity increases linearly from 0 to 15%), respective to different sensor lengths. The response of the electrical properties originates from the change in the lattice structure of monocrystalline silicon under the applied strain, enabling the degenerate optical phonons to split their vibrating frequencies, which can be measured as a shift by detecting the inelastic scattering of optical phonons via Raman spectroscopy (*29*). The presence of strain can enable the shift of the Raman frequency of monocrystalline silicon from their intrinsic peak (typically as ~520 cm^{-1}), where tensile strain results in the Raman peak shifting toward lower frequencies and compressive strain causes the peak to move toward higher frequencies. As shown in fig. S5, when the OSG device is subjected to an applied tensile strain of 0 to 15%, the Raman peak of the Si—Si bond gradually

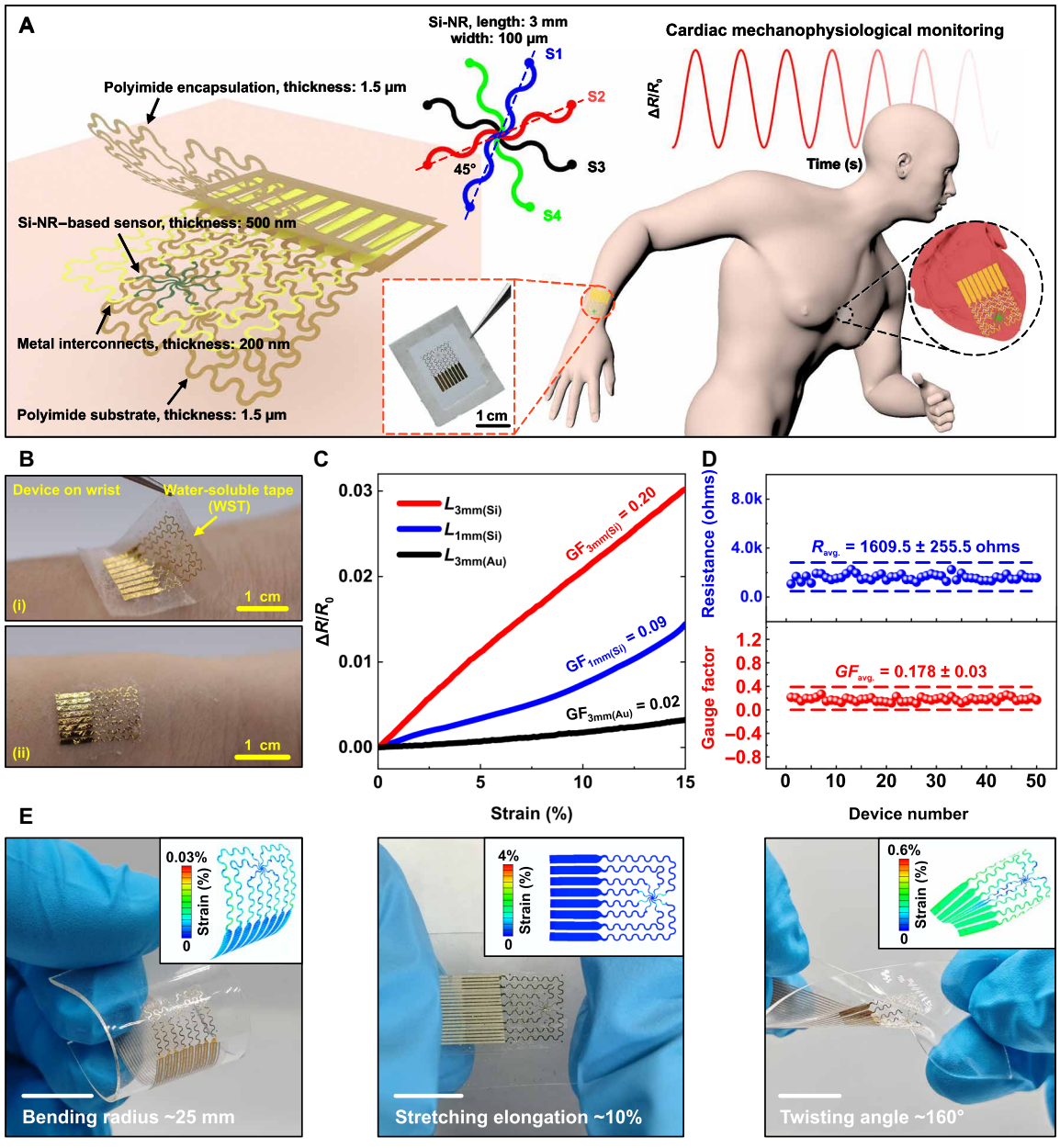

Fig. 1. Ultrathin Si-NR–based OSG devices for soft-tissue biomechanical monitoring. (**A**) Schematic illustration of the wearable and implantable application of OSG devices mounted on biological tissues to mechanically monitor physiological signals, such as cardiac pulse as an example (right). Top middle inset: The sensing area with four Si-NR–based sensors aligned with omnidirectional scale (from S1 to S4), with a 45° angle interval. Bottom middle inset: Image of the OSG sensor on a WST. (**B**) Photographs of a transferred OSG sensor laminated on wrist (i) before and (ii) after dissolving the WST. (**C**) The relative resistance change of a representative Si-NR–based sensor with different lengths (1 and 3 mm), compared to metal gauge (length, 3 mm) under identical strain condition. (**D**) Statistics on the resistance (blue dots) and the GF (red dots) among various Si-NR–based sensors collected from 50 different OSG devices, with an average value of 1609.5 ± 255.5 ohms and 0.178 ± 0.03, respectively. (**E**) Optical images of the OSG sensor under three different modes of mechanical deformation, including bending at the radius of 25 mm, stretching at the elongation of 10%, and twisting at the angle of 160°. Inset: FEA results of strain distribution across strain gauge for each corresponding state. Scale bar, 1 cm.

shifts from 520.09 to 514.24 cm^{-1}, consistent with the results from related studies (*29*, *30*). Details appear in text S1. Here, an important feature is on the GF of the sensor [GF_{sensor}; $GF = (\Delta R/R_0)/\varepsilon$, where ε represents the applied strain of the sensor]. Under the same applied strain condition, the GF of a 3-mm-long Si-NR yields a high $GF_{3mm(Si)}$ of 0.20, which greatly surpasses that of a 1-mm-long Si-NR [$GF_{1mm(Si)}$ of 0.09]. Other types of metal strain sensors of Au offer even lower values of GF [$GF_{3mm(Au)} = 0.02$] for a 3-mm-long NR, inferior to that of a Si-NR–based gauge by an order of magnitude. Figure S6 (A and B) presents the comparison of the measurement sensitivity of the Au film–based gauge and Si-NR–based sensors both with a length of 1 mm, indicating that the GF of the latter sensor (Si-NR, ~0.09) greatly surpasses that of the former sensor (Au, ~0.01), consistent with the previous studies (*18*, *31*).

As a consequence, Fig. 1D summarizes the results for the measured electrical resistance and the corresponding GF_{sensor} in the collection across 50 different OSG devices. The results suggest uniformity and consistency in the device performance across all the fabricated systems, with an average value of electrical resistance is 1609.5 ± 255.5 ohms, with that of the GF_{sensor} being 0.178 ± 0.03.

Taking the above key characteristics, the ultrathin strain sensor brings great application prospects for wearable and implantable medical devices to clinical diagnosis and treatment. Table S1 summarizes a detailed comparison between the proposed device as a strain sensor and a wide range of key material types such as traditional metal films, conductive hydrogels, and organic/inorganic materials, with various GFs, dimensions, stretchability, response time, and functions (*24*, *32*–*39*). By comparison, traditional metal film (i.e., gold) strain gauges offer limited GF. Other materials such as conductive hydrogels can yield extraordinary stretchability and higher GF, where challenges remain in low spatial resolution and measurement hysteresis (*32*). Alternatives, including organic films, nanowires/nanotubes, and two-dimensional materials (e.g., graphene and MXene), can provide excellent mechanical measurements with higher GF (even up to 10^2 to 10^3), with the potential to capture tiny motions (*33*–*37*). However, continuous efforts for these approaches focus on the improvement of measurement capabilities that typically suffer from device-to-device variation.

For the mechanical properties of OSG devices, Fig. 1E shows photographs of the device at various mechanical deformation states and corresponding theoretical simulation, which include bending (with a bending radius of 25 mm), stretching (with an elongation of 10%), and twisting (with an angle of 160°) on an artificial skin substrate (PDMS, 1 mm thick) to avoid the fracture. The internal strain distributions of the OSG devices under each state are analyzed using the finite element analysis (FEA) simulation. Under large strain (10 to 15%), the simulation demonstrates the maximum internal principal strains of 0.28 and 4.03% in metal interconnects and Si-NRs, respectively, well below fracture strain of gold film (~7%) and Si (~5%) (*31*, *38*–*40*), indicating the excellent flexibility and mechanical robustness of the OSG device. Details appear in text S2, table S2, and Materials and Methods. Differences between the applied and internal strains arise from ultrathin serpentine patterns of Si-NRs and metal interconnection to increase the path length and reduce internal strain concentration, and the mechanical stretchability of the OSG device is enhanced (*38*–*40*). Furthermore, the differences in elastic modulus and thickness between the PDMS substrate (millimeters in thickness) and Si/Au (nanometers in thickness) can result in the strain to concentrate within the PDMS substrate, with relatively less strain in the OSG device (*38*–*40*). Thereby, these results are crucial for preserving functional integrity and operational efficacy under various physical conditions, providing high-precision mechano-physiological measurements.

Experimental and computational analysis of the operational principles for device operation

The soft tissues of the human body are in continuous motion and adaptation, causing strains that vary in both direction and intensity (*41*). Compared to strain measurements solely in a single direction, capture of multi- and/or omnidirectional dimensions at a wide range of strain levels can offer clinical significance for human physiological sensing, such as complex movements of the skin and heart. In this context, the design constructs octopus-like shapes that can enable real-time monitoring of surface strain at an omnidirectional scale, as shown in Fig. 2A, thus allowing for intimate contact synchronous to tissue deformation.

Here, the FEA simulation can quantify the mechanical coupling within the device structure and thus assess the measurement capabilities. As an example, Fig. 2B shows the FEA simulation of the OSG device coupled onto an artificial skin (1 mm thick) under quasi-static conditions, where the tensile strain is applied to the substrate ($\varepsilon_{appl.}$) along the *y*-axis direction (red arrow; $\varphi_{appl.} = 0°$) with the intensities of $\varepsilon_{appl.}$ being 0, 5, and 15%, respectively, and $\varphi_{appl.}$ denotes the angle between the direction of the *y* axis and the applied strain. The strain distribution gradually goes up with increasing intensities of $\varepsilon_{appl.}$. According to the FEA simulation, the maximum strain in Si (~4.7%) is lower than the material fracture limit (~5%) (*31*, *38*–*40*), further proving the robustness of OSG devices. Each Si-NR–based sensor exhibits distinct mechanical responses; to be specific, S1 and S4 sensors experience notably larger strain compared to that of S2 and S3 sensors. The difference in strain distribution can lead to distinct measured signals of each sensor, which are related to intensities and direction angles of the applied strain.

To dynamically evaluate the measurement in a fixed direction, Fig. 2C illustrates the $\Delta R/R_0$ of the S1 sensor as a representative example under mechanical periodic cycles of $\varepsilon_{appl.}$ along the sensor direction. The results of measured $\Delta R/R_0$ follow exactly with the applied cyclic strain in terms of different intensities (from 0 to 15%, as shown in fig. S7A), with high measurement accuracy under each condition. Figure 2D summarizes the dependence of $\Delta R/R_0$ of the S1 sensor with different applied strain intensities of $\varepsilon_{appl.}$ from 0 to 15% and from 0 to 0.3%, respectively. The results show no notable creep effect during the full measurement ranges. In addition, cyclic mechanical tests with tensile strain up to 1000 cycles are performed, demonstrating excellent operational stability and low hysteresis (fig. S7B). The response and recovery time of the device are quantified at a millisecond level (80 ms; fig. S7C) that is adequate for physiological measurements, primarily due to the material properties of monocrystalline silicon. Figure S7D displays the stable mechanical response of the OSG device at a constant strain intensity but with varying rates. In addition, curved surfaces of the tissues such as the skin have only a minor influence on the measurements. As shown in fig. S8, the electrical resistance change (R/R_0) of a representative sensor stays constant when being attached to surfaces with different curvatures, demonstrating the feasibility of the device for the use of wearable and implantable electronics.

For the examination of the angular dependence of the individual sensor, $\varepsilon_{appl.} = 10\%$ is applied to the entire OSG device spanning clockwise across $\varphi_{appl.}$ from 0° to 90°. Figure 2E shows the $\Delta R/R_0$ of the S1 sensor as a function of $\varphi_{appl.}$ (blue dots). In addition, fig. S9A collects the results of $\Delta R/R_0$ of the other three sensors (S2, S3, and S4) as the angle of $\varphi_{appl.}$ ranging from 0° to 90°. All cases for these four sensors show consistency between theoretical modeling and experimental results. Figure S9B extends the scale from −90° to 90°. The results demonstrated that the maximum of $\Delta R/R_0$ of each sensor occurs at the angle aligned to the direction of the specific sensor. For example, as $\varphi_{appl.}$ increases, for S1 sensor, $(\Delta R/R_0)_{max}$ occurs right at the angle aligned to the direction of the S1 sensor ($\varphi_{appl.} = 22.5°$). Theoretically, $\varepsilon_{S1.}$ and $\varphi_{appl.}$ satisfy the function (details appear in fig. S10 and text S3)

$$\varepsilon_{S1} = \frac{\varepsilon_{appl.}\left[1+3\cos\left(2\varphi_{appl.}-45^{o}\right)\right]}{4} \quad (1)$$

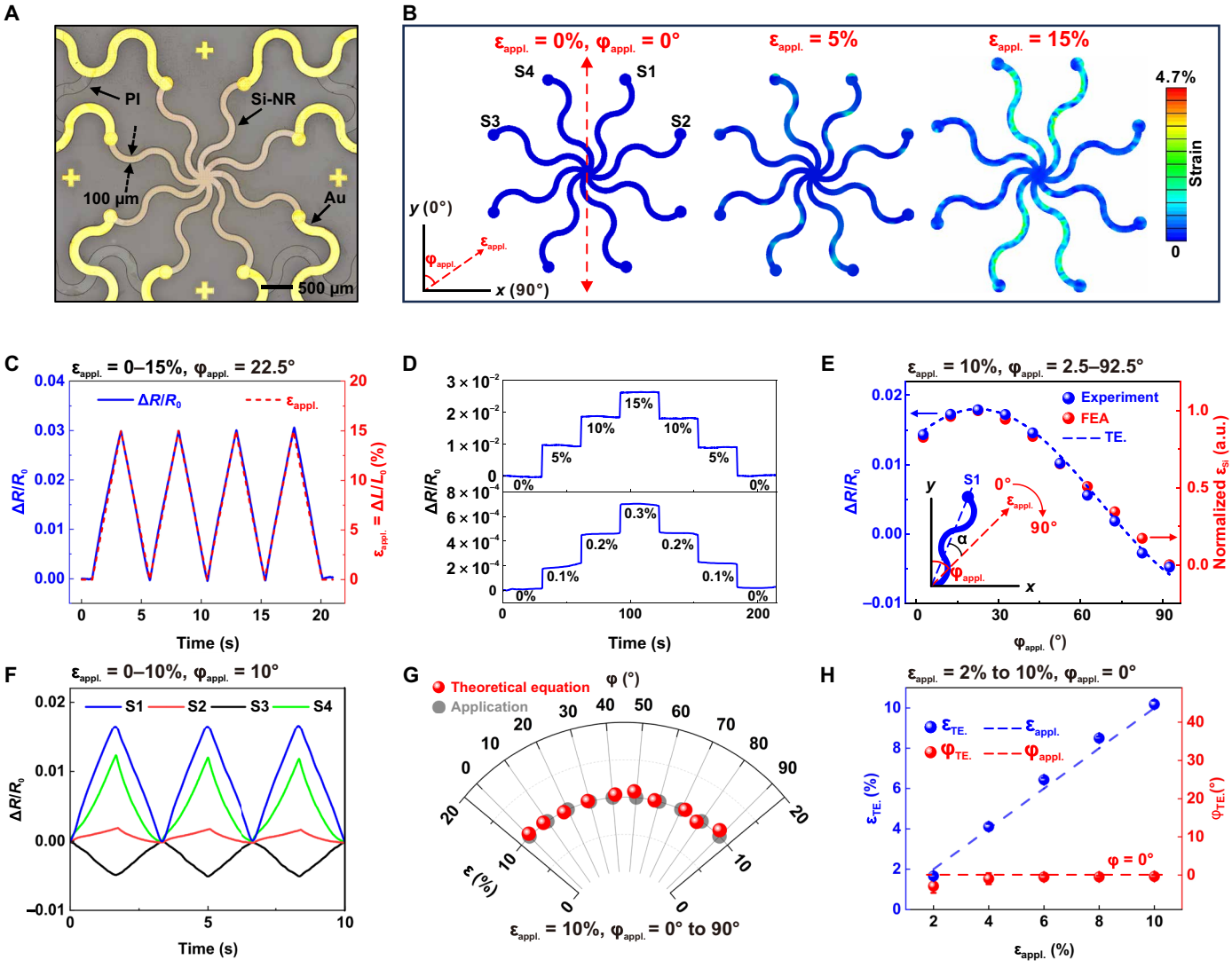

Fig. 2. Sensing characteristics of Si-NR–based OSG device. (**A**) Magnified optical image of the sensing area of Si-NR–based strain sensors. (**B**) FEA simulation results for the distribution of the maximum principal strain across the four Si-NRs on artificial skin substrate with 0, 5, and 15% stretching along the *y* axis. (**C**) Relative change in resistance of S1 sensor (blue line) corresponding to cyclic tensile strain (red dashed line) ($\varepsilon_{appl.}$ = 0 to 15% and $\varphi_{appl.}$ = 22.5°, along the direction of S1 sensor). (**D**) Relative resistance change of S1 sensor under a step tensile strain ($\varepsilon_{appl.}$ = 0 to 15% at 5% intervals and 0 to 0.3% at 0.1% intervals, respectively, and $\varphi_{appl.}$ = 22.5°). (**E**) Results of relative change in resistance of S1 sensor from experiments (blue dots), the theoretical equations (blue dashed line), and FEA simulation (red dots) results of normalized strain across silicon of S1 sensor, with applied strain at fixed intensity ($\varepsilon_{appl.}$ = 10%) as a function of clockwise direction angles $\varphi_{appl.}$. Inset shows the schematic illustration of $\varepsilon_{appl.}$. a.u., arbitrary units. (**F**) Response characteristics of four Si-NR–based sensors during cyclic strain ($\varepsilon_{appl.}$ = 0 to 10% and $\varphi_{appl.}$ = 10°). (**G**) Comparison between the applied strain (gray dots; $\varepsilon_{appl.}$ = 10% and $\varphi_{appl.}$ = 0 to 90°) and the results of strain detection from theoretical equations (red dots) based on the 45° angular coordinate system. (**H**) The determination of strain intensities ($\varepsilon_{TE.}$; blue dots) and direction angles ($\varphi_{TE.}$; red dots) from theoretical equations under an applied strain with various intensities (blue dashed line; $\varepsilon_{appl.}$ = 2 to 10%) at a fixed direction (red dashed line; $\varphi_{appl.}$ = 0°). Error bars correspond to the calculated SD from three measurements.

$\Delta R/R_0$ of the S1 sensor can be obtained by multiplying ε_{S1} with GF_{S1} (calibration of GF is shown in Materials and Methods). ε_{S1} experiences a transition from positive to negative (from tensile to compressive strain) once the angular interval exceeds 54.7°, resulting from the Poisson's ratio effect of the substrate (*42*). On the basis of the above theoretical equation (TE.), the change in the strain distribution of the S1 sensor can be obtained theoretically (blue dashed line). Overall, the results of experiments, FEA simulation, and theoretical equations appear in Fig. 2E, with $\Delta R/R_0$ of S1 sensor under $\varepsilon_{appl.}$ as a function of $\varphi_{appl.}$, all of which are in good agreement with each other.

Next, we would consider the mechanical response of the entire OSG device with four different sensors, under a specific dynamic condition. Figure 2F displays the real-time $\Delta R/R_0$ of each sensor (S1, S2, S3, and S4) under periodic strain of $\varepsilon_{appl.}$ ($\varphi_{appl.}$ = 10°). Results of the four strain sensors reveal the distinctive mechanical responses, where the S1 sensor illustrates the highest results because of the direction of the sensor aligned closest to the direction of $\varepsilon_{appl.}$. Therefore, the OSG device with four sensors across an omnidirectional scale can yield direction angle–sensitive measurements, thus resulting in capabilities for resolving and detecting both the strain

intensity $\varepsilon_{appl.}$ and the direction angle $\varphi_{appl.}$ under different conditions, which will be discussed subsequently.

On the basis of the direction angle–sensitive characteristics, an analytical system, which refers to the 45° angular coordinate system, can be established in Fig. 2G for resolving a randomized strain by the two adjacent strain sensors, thus supporting the determination of strain intensities and direction angles. For example, it is difficult to distinguish between two strains whose directions are symmetrical about the *y* axis: to be specific, $\varphi_{appl.} = 20°$ and $\varphi_{appl.} = -20°$ will produce the same change in electrical resistance for two vertically placed strain sensors, leading to an ill-posed strain calculation problem (*35*, *43*). As a solution, a 45° angular coordinate system in this case is proposed to restore the direction angle and the strain intensity by $\Delta R/R_0$ and GF of two adjacent sensors (details appear in fig. S11 and text S4). Note that smaller angular intervals, such as a 15° design (with 12 Si-NR–based sensors), would greatly enhance directional resolution by decreasing the angle between the applied strain and each sensor, thus improving measurement sensitivity. However, this increases the complexity of fabrication with careful processing of transfer printing and complicated metal wiring, thus posing challenges for system integration that would affect human daily activities. As opposed to smaller angular interval designs, larger angular interval patterns would reduce the measurement precision, as shown in fig. S12. As discussed in text S3, eq. S3 describes the relationship between the strain along the sensor direction (S1 sensor as an example) and the applied strain, where ε_{S1} decreases to negative as the angular interval of α exceeds 54.7°. In this context, larger angular intervals, such as 60°, can lead to a reduction of GF from 0.2 (as for 45° interval) to 0.018 by an order of magnitude.

Define $\varphi_{TE.}$ as the theoretically calculated direction angle and $\varepsilon_{TE.}$ as the calculated strain intensity between two adjacent sensors based on the following theoretical equations. These values can be derived as follows (details appear in text S4)

$$\varphi_{TE.} = 22.5° + \alpha = 22.5° + \arctan\left(\frac{-3+\sqrt{2}\sqrt{4\bar{\varepsilon}^2+\bar{\varepsilon}+4}}{1+2\bar{\varepsilon}}\right) \quad (2)$$

$$\varepsilon_{TE.} = \frac{4\left(\frac{\Delta R/R_0}{GF}\right)_{S1}}{1+3\cos(2\alpha)} = \frac{4\left(\frac{\Delta R/R_0}{GF}\right)_{S2}}{1+3\sin(2\alpha)} \quad (3)$$

where α is the angle between the direction of tensile strain and the sensor (S1 for example) and $\bar{\varepsilon}$ is defined as $\varepsilon_{S2}/\varepsilon_{S1}$, i.e., $[(\Delta R/R_0)_{S2}/GF_{S2}]/[(\Delta R/R_0)_{S1}/GF_{S1}]$, when $\varphi_{appl.}$ is between 22.5° and 67.5° (S1 and S2). With a fixed applied strain $\varepsilon_{appl.} = 10\%$ imposed in different direction angles ($\varphi_{appl.}$ changes from 0° to 90°; gray dots), the scalable measured strain for an omnidirectional detection can be obtained by Eqs. 2 and 3. For $\varphi_{appl.}$ at other angle ranges, $\varphi_{TE.}$ and $\varepsilon_{TE.}$ can be calculated using the corresponding two adjacent Si-NRs. In this way, Fig. 2G shows the calculation results of $\varphi_{TE.}$ and $\varepsilon_{TE.}$ (red dots) based on the 45° angular coordinate system and the actual applied strain $\varphi_{appl.}$ and $\varepsilon_{appl.}$ (gray dots), verifying the consistency. In this manner, these methods can provide high-precision measurements of the applied strain at an omnidirectional scale. Furthermore, Fig. 2H summarizes the measurement capabilities of the OSG device at a condition that involves changes in applied strain intensities ($\varepsilon_{appl.}$ from 2 to 10%) at a fixed angle ($\varphi_{appl.} = 0°$). The results of $\varphi_{TE.}$ (red dots) and $\varepsilon_{TE.}$ (blue dots) are in agreement with $\varphi_{appl.}$ (red dashed lines) and $\varepsilon_{appl.}$ (blue dashed lines), respectively. The findings above suggest the potential use of OSG devices for high-accuracy detection of strain intensity and direction angle, at spatial measurement scale for omnidirectionality across biotissue surfaces.

In addition, the miniaturization of the Si-NR–based sensor can affect the spatial resolution and measurement sensitivity of the OSG devices. To illustrate this point, we fabricate two groups of OSG devices with Si-NR lengths scaled from millimeters to micrometers (2 mm and 600 μm, respectively) in a 2 × 2 array design, as shown in fig. S13 (A and B). Figure S13 (C and D) presents the results of spatial maps with strain intensities and direction angles, in terms of different scales of Si-NR lengths of 2 mm and 600 μm, respectively. Details can be found in text S5. Figure S13E summarizes the GF of the OSG devices with respect to different scales ranging from millimeter scales to micrometer levels; the results of which indicate that increasing the spatial resolution also reduces the GF, consistent with the results in Fig. 1C.

These findings suggest that the OSG device provides scalable designs with high resolution, stable performance, and rapid response time (millisecond level) under dynamic conditions, with the potential use for high-accuracy detection of strain intensity and direction angles in monitoring skin deformation. However, all these highly dynamic conditions that involve time-dependent changes of strain direction would yield challenges for the existing system functions with technical requirements of shorter calculation duration and larger datasets. Future efforts for system optimization with the use of machine learning algorithms will provide powerful application potential.

Integration as bioresorbable platforms for biocompatibility characteristics and stable operation

The biodegradability of electronic devices refers to their ability to safely break down within living organisms, such as the cardiovascular system, nervous system, and others, through natural metabolic processes. Such a characteristic eliminates the need for a follow-up second surgery operation to remove the implanted device (*44*, *45*). Figure 3A presents a schematic illustration of the OSG device with the use of biodegradable materials, mounting on epicardium for cardiac mechanophysiological signal monitoring in an omnidirectional fashion. Here, a thin, bioresorbable layer of molybdenum (Mo) can serve as metal interconnections. Stretchable and fully biodegradable elastomeric polymer layers of bioresorbable dynamic covalent polyurethane (b-DCPU) can integrate with OSG devices, in thin-film forms that not only serve as the front encapsulation but also serve as the bottom substrate (each of 50-μm thickness). Detailed information about the fabrication of biodegradable devices can be found in Materials and Methods and fig. S14.

Here, the top of Fig. 3B shows the real-time measurement collection for in vitro test under cyclic stretch/release ($\varepsilon_{appl.} = 10\%$ and $\varphi_{appl.} = 0°$) (S1 sensor as example), which demonstrates that the relative electrical resistance change of the bioresorbable OSG device is in linear response to the applied strain. According to the 45° angular coordinate system established in Fig. 2G, here, the results measured within the adjacent two sensors (which refer to S1 and S4 sensors) can derive the exact strain onto the OSG device ($\varepsilon_{TE.}$ and $\varphi_{TE.}$). From the Eqs. 2 and 3 displayed in Fig. 2, $\varepsilon_{TE.}$ and $\varphi_{TE.}$ showcase well-consistent results with $\varepsilon_{appl.}$ and $\varphi_{appl.}$ (10.72% and 1.15°), respectively, which shows the reliability of strain detection. In parallel, the bottom of Fig. 3B shows in vivo recording that directly laminates on a living rat heart for continuous

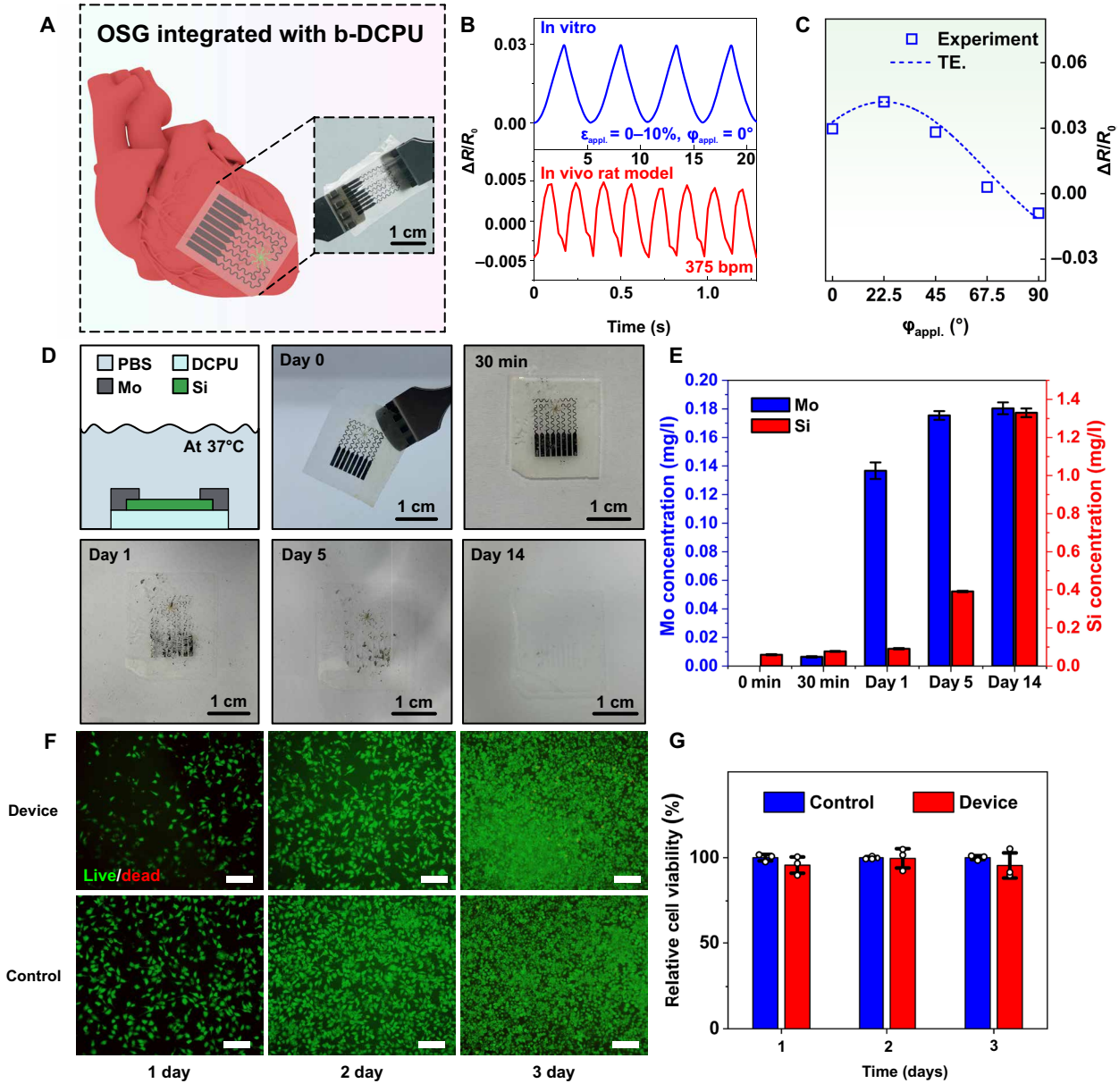

Fig. 3. Biodegradable, stretchable, and biocompatible Si-NR–based OSG devices. (**A**) Schematic diagram of the biodegradable and stretchable strain gauge for cardiac signal monitoring. Inset: Image of the transient OSG device under stretching. (**B**) Relative change in electrical resistance of the strain gauge during in vitro (under cyclic tensile strain; $\varepsilon_{appl.} = 0$ to 10% and $\varphi_{appl.} = 0°$) and in vivo tests on the cardiac surface of a living rat, respectively. (**C**) The experimental results (blue square) and results from theoretical equations (blue dashed line) of $\Delta R/R_0$ of biodegradable OSG device under different $\varphi_{appl.}$ values (from 0 to 90°) with $\varepsilon_{appl.} = 10\%$. (**D**) Photographs of the device degrading in PBS solution (pH 7.2 at 37°C) at different timescales. (**E**) Concentrations of Si and Mo as a function of duration immersed in PBS solution (pH 7.2 at 37°C). Error bars correspond to the calculated SD from three measurements. (**F**) Fluorescence microscopy images of live/dead-stained L929 cells cocultured with the OSG device (top) and without devices (bottom) as control samples. Scale bars, 100 μm. (**G**) Relative viability of L929 cells as a function of culture time (1, 2, and 3 days), in comparison with control groups. Error bars correspond to the calculated SD from three measurements.

tracking of cardiac diastole/systole cycles with a heart rate of 375 beats/min (bpm), indicating the feasibility of such a biodegradable, stretchable device for the use as cardiac implants (details appear in the following section). Figure 3C shows the omnidirectionality of these biodegradable OSG devices, where the strain measurement with variable direction angles is in good agreement with those in Fig. 2E (taking the S1 sensor as an example).

Specifically, sensing components of silicon-based devices exhibit inherent solubility in biofluids such as phosphate-buffered saline (PBS) solution, with variable dissolution rates reported in biological fluids within different conditions from the previous publication (*46*). Ultrathin layers of Mo materials (200 nm thick) provide excellent biodegradable characteristics in the human body (*47*). Figure 3D illustrates the soak test of a representative device platform on a

single-sided b-DCPU substrate without top encapsulation, continuously immersed in PBS (pH 7.4) at a body temperature of 37°C. Hence, the device components of Si/Mo are directly exposed to PBS solution in an accelerated mode and dissolve completely within 14 days, indicating the complete biodegradability of the functional electronic platforms. The b-DCPU also exhibits fully biodegradable characteristics, but at a relatively slow rate, resulting in a long timescale for complete dissolution in biofluids. As a demonstration, fig. S15 shows the OSG devices embedded in double layers of b-DCPU (50 μm thick), with effective protection of the OSG devices for over a month in PBS at 37°C, in good agreement with previous publication (*48*). In an ideal scenario, the OSG device can remain functional until the complete dissolution of the encapsulation or substrate layers of b-DCPU, where these materials can offer controllable dissolution rates depending on the content of polyethylene glycol. Other encapsulation candidates, including alternative encapsulation materials such as polylactic acid–glycolic acid and polylactic acid, can also demonstrate biodegradable properties to control degradation windows (*49*). Overall, these results indicate the operational stability of the OSG device for in vivo use, with a projected lifetime of many months in our case.

As the evidence to support the biocompatibility of the wearable/implantable devices, the inductively coupled plasma optical emission spectrometry (ICP-OES) measurements can yield important information. During the soak tests within PBS solutions (Fig. 3D), the ICP-OES results present the elemental species of the dissolved products and their concentrations that are released in biofluids surrounding the implants during continuous immersion. In detail, Fig. 3E illustrates the evaluation of the concentration of elements of Mo and Si (major constituent materials of the OSG device) after the electronic platform fully dissolved in PBS solution across different timescales. The results indicate that the concentrations of Mo and Si yield saturation 5 days after immersion, while all remain at a low level for safe operation, which supposes the excellent biocompatibility of our degradable OSG as stable implants.

On the other hand, Fig. 3F shows the associated biocompatibility test on cell cytotoxicity experiments, as further proven evidence beyond the in vitro soak tests of ICP-OES measurements. Images of stained live (green) and dead (red) cells (mouse cardiac fibroblasts, L929) cocultured right with our biodegradable OSG devices for sufficient timelines of 1, 2, and 3 days obtained via fluorescence microscopy. Figure 3E displays the relative viability of L929 cells using a cell counting kit-8 (CCK-8) assay. The comparison between the samples (red in Fig. 3G) and control samples (which refer to the cells cultured without OSG devices; blue in Fig. 3G) indicates that there is no substantial decrease in the relative cell viability between these two groups. Further histological analysis that includes hematoxylin and eosin staining and Masson's trichrome staining was performed on the cardiac tissues of the rat models after 7-day implantation of the OSG devices, as shown in fig. S16 (A and B), respectively. Here, the results indicate an absence of tissue fibrosis or inflammation, consistent with the previous related literature (*50*). Taken in combination with cell cytotoxicity experiments and histological analysis of the cardiac tissues, these results indicate that the biodegradable OSG devices can offer nontoxic properties and are well compatible with cardiac tissues, suggesting the potential for use as long-term implants for in vivo stable operation. Taken in combination with cell cytotoxicity experiments, these results indicate that the biodegradable OSG devices are nontoxic and well compatible to cardiac tissue, suggesting the potential for the use as long-term implants for stable operation.

Wearable applications in real-time monitoring of mechanophysiological signals for both human and animal models

Figure 4A illustrates the OSG devices that serve as wearable electronics to monitor mechanophysiological signals, with an ultrathin structure (Fig. 1A) in noninvasive manner that includes measurements for IOP of eyeballs, facial expression, carotid and radial pulses, etc. In all these cases, the mechanism involves continuous measurements via the ultrathin platforms of the OSG device mounted on soft-tissue surfaces to detect physiological activities with isotropically (e.g., IOP and carotid and radial pulses) or anisotropically (e.g., facial movements) distributed mechanical strain, all of which can be captured by the Si-NR–based sensors under dynamic conditions in an omnidirectional scale.

Figure 4B indicates the approach that enables the monitoring of IOP by detecting mechanical strain with isotropic distribution on the surface of a porcine eyeball. The OSG device is located at the center regions of the eyeball surface, and we take the S1 sensor as an example for measurement. For the experimental setup, the regulation of IOP is achieved through the control of the flow amount of water injected into and withdrawn from the ocular anterior chamber. The S1 sensor can allow for the detection of subtle strains that can be converted to the monitoring of IOP; results of which indicate the capability of identifying pressure variations within the range of IOP (13 to 27 mmHg) in porcine eyes (Fig. 4C). By comparison, commercial IOP sensors (Testo 510i) also yield similar results (red dashed line) consistent with those of OSG devices (blue line), suggesting the feasibility of the OSG device for monitoring the IOP of eyeballs. As the strain distribution, in this case, is isotropic across an omnidirectional scale at the eyeball surface, the other strain sensors (S2, S3, and S4) of the OSG device yield similar measurement results with uniformity. Upon application of a PDMS substrate as the biotic/abiotic interface, the OSG device can enable multiple reuses for monitoring IOP while maintaining performance. Figure S4D shows the OSG device with PDMS accurately measures the IOP of a porcine eyeball.

Further to monitoring IOP strain, another example in Fig. 4D shows the use of the OSG devices for repetitively recognizing facial expressions in a specific direction, where the contraction and relaxation of facial muscles (angulus oris) can yield an anisotropic strain distribution under dynamic conditions. Here, the OSG device is positioned near the angulus oris of a volunteer human individual, with S2 sensor aligned to the vertical axis of the face (inset of Fig. 4D). For instance, raising angulus oris upward (i.e., happiness) can generate tensile stain that increases $\Delta R/R_0$ of the S2 sensor, as opposed to falling angulus oris downward (i.e., sadness) that can lead to compressive strains that results in the decrease in $\Delta R/R_0$. Real-time monitoring of cyclic facial movements yields opposite output responses during periodic happy/sad expressions. Furthermore, the OSG device can offer potential use for reading recognition with directionality. Figure S17 presents the recording data of the device in terms of different pronunciations associated with letters, words, and short phrases. The omnidirectional capability enables the OSG devices to capture these strain changes and their directions during the movement of mouths. In addition to facial characterization, similar experiments on the throat surface, as shown in fig. S18, demonstrate that the OSG device enables the monitoring of cyclic swallowing movements during continuous measurements.

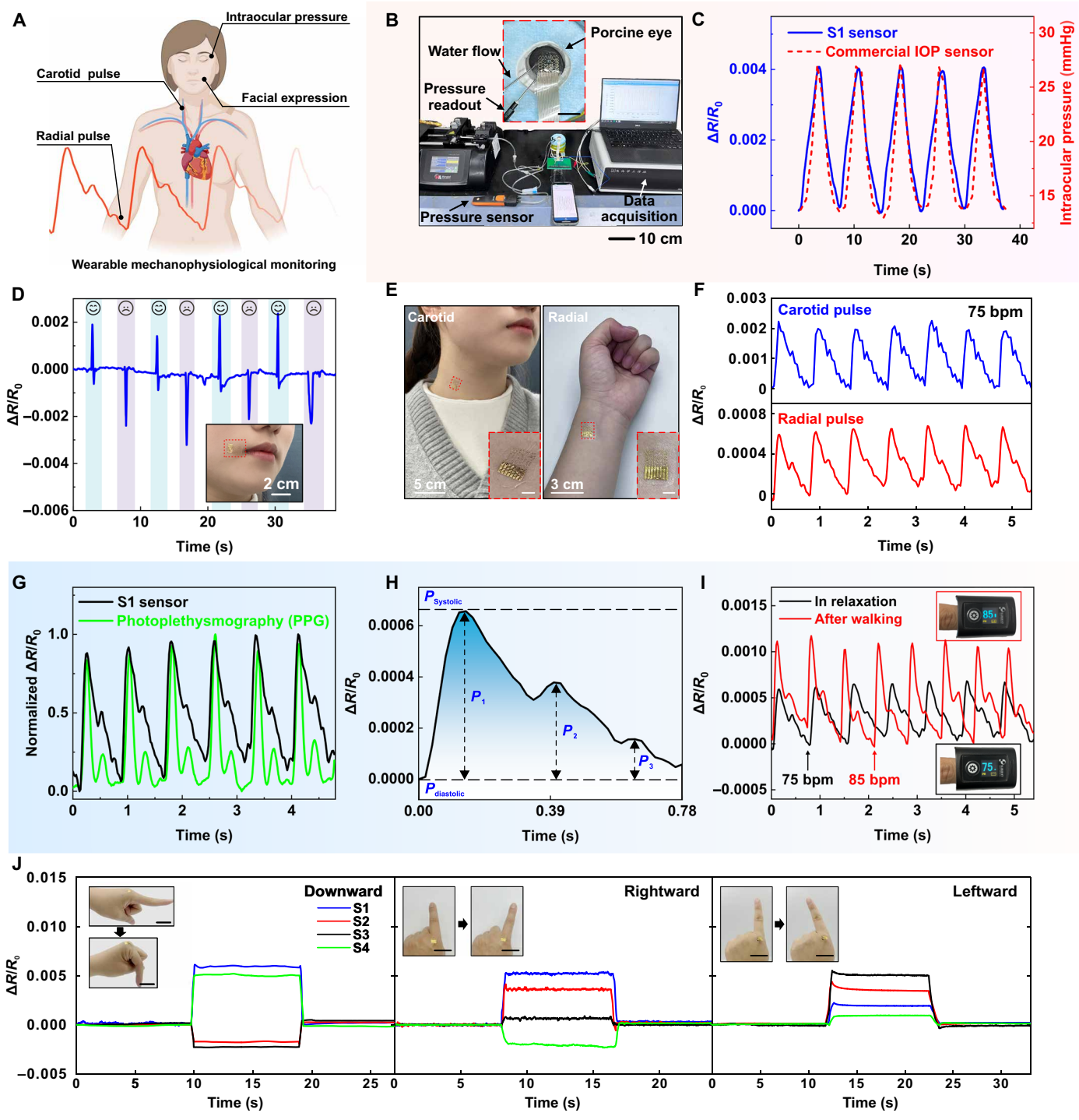

Fig. 4. Wearable applications in mechanophysiological monitoring of human body and animal models. (**A**) Schematic illustration of mechanophysiological monitoring for the human body. (**B**) Experimental setup for monitoring IOP in the porcine eye. (**C**) Relative change in electrical resistance of a representative strain sensor (S1) of the OSG device (blue line) and result from a commercial pressure sensor (red dashed line) under cyclic variation of IOP (13 to 27 mmHg). (**D**) Real-time measurement for repetitive facial expression detection as the corner of the mouth rises or falls. Inset: Photograph of a strain gauge attached to the corner of the mouth. (**E**) Photograph of the OSG devices attached to the neck (left) and the wrist (right) for artery pulse pressure measurements. Scale bars, 0.5 cm (insets). (**F**) Relative change in electrical resistance collected by a representative strain sensor (S1) responds to radial artery (red) and carotid artery (blue) pulse pressure. (**G**) Normalized relative change in electrical resistance (black) compared with the results from the commercial sensor (green) during pulse pressure monitoring. (**H**) Single radial artery pulse pressure waveform measured with the Si-NR–based sensor comprising three peaks (P_1, P_2, and P_3). (**I**) Relative change in electrical resistance during monitoring in relaxation (black) and after walking (red). Insets show the results measured with a commercial heart rate monitor. (**J**) Detection of different motion modes of finger joint based on OSG device. Scale bars, 3 cm.

As for the daily use of wearable electronic platforms, human motion artifacts are a noteworthy issue for precise measurements of the biomechanical sensors (*51*). To illustrate this, we further investigated the application of our OSG devices as skin-wearable electronics to human volunteer individuals during slow running and riding on a bike, as summarized in fig. S19 (A and B), respectively. We performed our OSG devices for monitoring the volunteer's carotid pulsation point during slow running and for capturing finger motion during riding (details appear in Materials and Methods). Under both dynamic conditions, the results show stable measurement capabilities of our OSG device under motion artifacts, consistent with other previous publication (*52*). Alternatively, fig. S20 presents the mechanical evaluations of OSG devices mounted on the back of the neck during nodding in cycles, with stable measurement results both under dry and sweaty skin states. These findings suggest the broad utility of a wide range of wearable electronics for continuous monitoring of the mechanical properties of biological soft tissues.

In addition, monitoring pulse waves of human individuals, highlighted in Fig. 4 (E to I), can serve as a direct reflection of the cardiovascular status of the living body and provide an efficient means for real-time, noninvasive diagnosis of atherosclerosis, hypertension, and other cardiovascular conditions (*53*, *54*). Specifically, Fig. 4E demonstrates the application of the Si-NR–based sensor in pulse monitoring of both radial and carotid arteries at different regions of the living body. The principle is based on the rhythmic contraction of the heart, which propels blood through the arteries, leading to variations in blood vessel diameter and induced periodic deformation of the skin surface (*54*). For the experimental setup, because of the isotropic mechanical deformation across the skin, we select the S1 sensor of the OSG device as a representative example to evaluate the pulse measurements. Figure 4F shows the pulse waveforms of both radial and carotid arteries obtained with the OSG device (~75 bpm). The results reveal that the magnitude of the pulse signal $[(\Delta R/R_0)_{max}]$ from the carotid artery is higher than that of the radial artery, consistent with expectation as the carotid artery is closer to the heart. As a comparison, the pulse signals are measured by conventional metal strain gauges (Au) with the same device geometry as that of the Si-NR–based sensor (fig. S21A). The larger magnitude of $(\Delta R/R_0)_{max}$ indicates that the sensitivity of Si-NR–based sensor is three times higher than that of metal strain gauge (fig. S21B), consistent with the results of GF shown in Fig. 1C. Furthermore, Fig. 4G exhibits the comparative measurements based on a commercial photoplethysmography sensor (Pulse Sensor, Your Cee Co. Ltd.), matched with peak positions of the waveforms to those of OSG devices. Unlike the piezoresistive effect of the OSG devices, the measurement principles of photoplethysmography sensors are attributed to light scattering through the skin and underlying tissues (i.e., blood vessels) for detection of hemodynamics, thereby leading to slight differences in the measured signals of the pulse, as shown in fig. S22 (*55*).

Figure 4H displays an example of a complete radial pulse waveform by use of S1 sensor collected from a volunteer human individual (25 years old), consisting of three distinct peaks: the percussion wave (P_1), the tidal wave (P_2), and the diastolic wave (P_3), respectively (*56*). The P_1 arises when blood flow is ejected during the systole of the left ventricle (LV), reflecting the difference between the pressure of the heart during systole ($P_{systole}$) and that at the end of diastole ($P_{diastole}$). The P_2 and P_3 arise from the reflection of blood flow in the hand and lower body, respectively (*57*). As a consequence, the complete waveform can yield the radial artery augmentation index ($AI_r = P_2/P_1$) and the radial diastolic augmentation index ($DAI_r = P_3/P_1$) (*58*). Specifically, the results of Fig. 4H yield measurements of AI_r and DAI_r as 0.58 and 0.23, respectively, well consistent with those healthy human individuals (ages under 35, e.g., $AI_r = 0.60$ and $DAI_r = 0.30$), as reported in the previous researches (*59*, *60*). These parameters can provide useful clinical information as the basis of monitoring human health care such as vascular stiffness and blood pressure. For example, disorders of vascular sclerosis can lead to a decrease in artery elasticity, typically with an increase in the amplitude of the AI_r and DAI_r (*59*).

Beyond it, the characterization of the change of biological signals such as pulse rate is of interest, particularly for monitoring of physiological signals associated with human kinesiology. An example in Fig. 4I demonstrates the OSG device on the wrist of a volunteer human individual for real-time recording of the radial pulse both in a relaxed state and after a continuous motion state of rapid walking. Here, the real-time pulse monitoring after walking reveals an obviously higher pulse rate (85 bpm) and pulse amplitude ($\Delta R/R_0$ as 0.1%, indicated by P_1-wave amplitude); both of which surpass those at relaxation state (rate of 75 bpm and $\Delta R/R_0$ of 0.065%). As a comparison, we also exploit a commercial finger oxygenator (LEPU PC-60F; inset of Fig. 4I) as a reference; the results of which as shown in the inset of Fig. 4I yield 75 bpm for the relaxation state and 85 bpm for states after walking, consistent with those of the OSG device.

Figure 4J highlights omnidirectional measurement capabilities for capturing complex human motion (i.e., gesture detection), where human joints such as fingers exhibit complex movements (*61*). In this manner, we mounted the OSG device onto the finger joint of a human volunteer individual for real-time monitoring of different gestures. Insets correspond to the optical images of each gesture, including downward, leftward, and rightward. The measurement results show distinct changes in the electrical resistance responses for each gesture. Furthermore, a combination of machine learning systems with multiple sensor arrays can support the recognition of different modes of body motion. As an example, four OSG devices in a row that separately mount on the hand/finger joints at the index, middle, ring, and little fingers of a human volunteer individual can real-time capture different gestures including the numbers "1," "2," "3," and "4", respectively, with distinct output signals of $\Delta R/R_0$ of S1 sensor of each device owing to strain distribution across the multisensor array (fig. S23A). A machine learning system using a multilayer perceptron neural network enables the recognition of various gestures (*62*), suggesting potential use by achieving a high recognition rate and prediction accuracy of the algorithm in fig. S23 (B to D). Details are available in the text S6.

Implantable electronics for determination of cardiac abnormalities as disorder diagnosis

Cardiac-related diseases, such as arrhythmogenic activity, pose a notable risk to human health (*10*, *63*, *64*). Of particular interest is the direct and continuous monitoring of the cardiac surface mechanics without impeding its normal function, at an omnidirectional scale across tissue surfaces. Here, for precise measurements, the OSG devices in ultrathin structure (Fig. 1A) can yield excellent stretchability as developed in this study, thus allowing mechanical compliance with conformal contact to time dynamic surfaces under continuous deformation of cardiac tissue, serving as the basis for a stable measurement interface. Low bending stiffness is also critically

important in the system's feature for being flexible, fully implantable, and stretchable with minimal invasiveness, compatible with cardiac deformation, and stable operation in vivo, to circumvent the limitations of conventional rigid, planar approaches such as commercial pacemakers. In many cases, cardiac disorders involve abnormal deformation with both isotropic and anisotropic strain distributions across the heart surface. Here, as in Fig. 5, we report the use of OSG devices for monitoring the mechanics of hypoxia and MI as representative examples of cardiac disorders.

An in vivo test of a living rat model appears in Fig. 5A. The serpentine design of the strain sensor of the OSG device facilitates the adaptation to the continuous deformation of the beating heart (strain ranging from 10 to 20%). Specifically, cardiac contraction at end-systole refers to a decrease in $\Delta R/R_0$ of OSG device (compressive strain), while myocardium relaxation and ventricle expansion at end-diastole refer to increased $\Delta R/R_0$ of the device (tensile strain), as shown in Fig. 5B. Next, Fig. 5C demonstrates the real-time recording of S1 sensor, for example, to measure strain across the cardiac surface, where the periodic deformation of the OSG devices, particularly the Si-NR–based sensors, occurs simultaneously with the constant expansion/contraction of the heart. Under normal conditions, the strain induced by cycles of expansion/contraction can be considered isotropic; thus, the OSG device is placed at the LV as the y axis of the device is aligned with the cardiac long axis. The signal of $\Delta R/R_0$ exhibits periodic variations during implantation onto the cardiac surface. Here, the magnitude of $\Delta R/R_0$ yields a peak-to-peak value of 0.6% that can be defined as $\Delta R_{max}/R_0$, where the ΔR_{max} corresponds to the difference between the electrical resistances of the sensor at end-diastole and end-systole ($\Delta R_{max} = R_{diastole} - R_{systole}$). In this case, measurement results indicate the frequency that stands for the speed of heartbeats of the rat model, measured as 375 bpm.

In this manner, the OSG device can serve as an implantable cardiac patch in direct, conformal contact with the epicardium for monitoring its mechanical properties, which enables the detection of cardiovascular conditions, particularly for the use of pathology diagnosis, such as cardiac arrhythmias (Fig. 5D) and MI (Fig. 5E). A demonstrated example in Fig. 5D is a model of arrhythmias caused by hypoxia that refers to a common heart disease, which often involves the isotropic change of strain distribution during the pathology. This disease is established by removing the respiratory intubation for oxygen supply after open-heart surgery. Similarly, we take the S1 sensor as an example. Comparative data of continuous recording in the normal state (blue lines) and disease state (red lines) appear on the left of Fig. 5D, respectively. Long-term hypoxia can lead to reduced myocardial contractility, slow heart rate, and decreased blood output from the heart, which may cause degeneration and necrosis of cardiac muscle cells (*65*). As expected, the results of the arrhythmias/hypoxic state exhibit lower heart rate (200 bpm) by a substantial decrease compared to that under normal state (330 bpm), as shown in right of Fig. 5D. Simultaneously, a notable reduction in cardiac beating amplitude can be observed, resulting in a decrease in the amplitude of recording signals of OSG devices (0.12% compared to 0.55% under the normal state).

Another example of MI typically corresponds to the obstruction of different or combined blood vessels, such as the left anterior descending (LAD), right coronary artery (RCA), and left circumflex (LCX) in clinical practice (*66*). A key feature of this disorder can induce degradation of the extracellular matrix and progressive thinning/dilation of the ventricular wall within the infarct regions, thus leading to anisotropic changes of strain distribution, and particularly an attenuation of cardiac biomechanical properties in certain specific directions such as deterioration in amplitude and frequency during periodic contraction/expansion along the blocked vessels (*67*–*69*). Therefore, rapid localization of infarcts and related vessels is of high significance for subsequent timely treatment or cardiac surgery.

We used a classical MI model using living rats through ligation of the LAD with areas of heart apex along with the anterior wall of the LV (which refers to "LAD-apex" direction) affected by infarct in Fig. 5E. Figure 5F provides an illustrative scheme of two-dimensional strain distribution of the apex regions during MI states of the rat model, with the center of OSG devices directly positioned onto the apex and with four sensors aligning with different directions to various regions of the heart. Here, S1, S2, S3, and S4 are oriented along the direction from RCA to LAD (RCA-LAD), from RCA to LCX (RCA-LCX), from LAD to LCX (LAD-LCX), and from the apex to LAD (LAD-apex; red dashed line), respectively. Figure 5G shows an image of an OSG device laminated seamlessly on the epicardium of the living rat (movie S1).

The measurements via OSG devices can provide the capabilities of determination and identification of disease orientation/site associated with the MI pathology. Figure 5H records the signals measured by the OSG device along four different directions under the normal (left) and the MI states (right) of the rat model, respectively. In all the cases for omnidirectional sensing, results suppose a substantial reduction in amplitude and frequency of the signals at the pathological direction (here refers to the direction from LAD to apex in the ligation of LAD), owing to the deceleration in the heartbeat rate and weakening of the heart's ability for systole and diastole. Under normal conditions, the four sensors present the same level of output. As the MI disorder occurs, a remarkable reduction of the measured signals can be detected through the sensor oriented along the direction from LAD to apex (S4 sensor in this case) in Fig. 5H, leading to a $\Delta R_{max}/R_0$ of 0.17% compared to the average values of 0.32% collected from the other three sensors, where the ΔR_{max} corresponds to the peak-to-peak difference between the electrical resistances of the sensor at diastole/systole cycles. These results indicate the direction of the S4 sensor is aligned with the pathological orientation of the infarct. As a consequence, Fig. 5I summarizes the $\Delta R_{max}/R_0$ between the normal conditions and MI states, indicating that the strain along the pathological direction (S4 sensor) presents a higher reduction of $\Delta R_{max}/R_0$ of ~70% compared to those of ~35% from the other three sensors.

In addition to the direction-sensitive characteristics, OSG devices also demonstrate measurement capabilities for localization of the disorder-related regions. Figure S24 adopts the OSG device on the regions of right ventricle (RV) and LV; however, $\Delta R_{max}/R_0$ values of the four different directions (from S1 to S4 sensors) remain in a similar level (average value of 0.55% for RV and 0.30% for LV) with minor changes, indicating no orientation difference of measurement results in RV and LV regions compared to apex region where the MI occurs. These findings suggest system capabilities of the importance of OSG devices for monitoring cardiac-related diseases and identifying disorder regions/directions induced by arterial vascular infarcts. Overall, as a comparison with simple configurations with individual

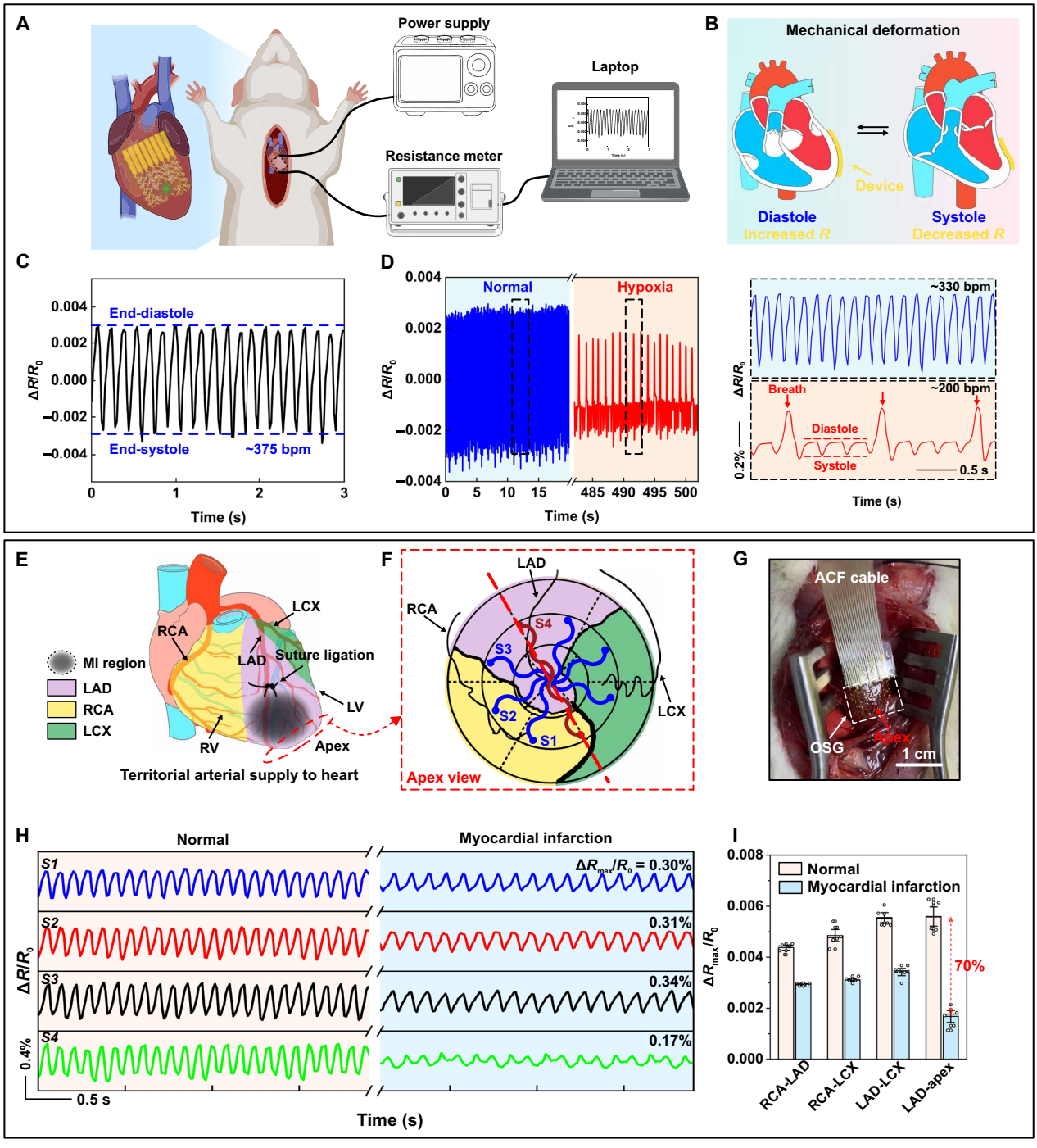

Fig. 5. In vivo cardiac mechanophysiological monitoring. (**A**) Schematic illustration of the sensing mechanism, in which the OSG device is laminated on epicardium to detect cardiac strain and the electrical resistance changes are captured and transmitted to laptop. (**B**) Measurement mechanism of the OSG device deforming with the expansion and contraction of the heart during cycles of diastole/systole. (**C**) Relative change in resistance of a representative Si-NR–based sensor (S1 sensor) of the OSG device during sinus rhythm monitoring. Here, the peak-to-peak magnitude of electrical resistance change of the S1 sensor corresponds to $\Delta R_{max}/R_0$ as of 0.6%, where ΔR_{max} can be defined as the difference between the electrical resistances of the sensor at end-diastole and end-systole, respectively. (**D**) Left: Relative change in electrical resistance of OSG device under normal (left) and hypoxic (right) conditions, respectively. Right: Comparison between normal and hypoxia conditions in a magnified view, where the diseased state corresponds to lower heart rates and beating amplitudes. (**E**) Schematic illustration of territorial arterial (LAD, RCA, and LCX) supply to heart and region of MI induced by ligation of LAD. (**F**) Schematic diagram of application of the OSG device laminated on the apex of the heart to detect MI. (**G**) Photograph of the OSG device mounted on the apex of the rat. The signal is derived from the anisotropic conductive film (ACF) cable. (**H**) Relative change in electrical resistance of four Si-NRs in healthy and MI states, respectively. (**I**) The comparison of $\Delta R_{max}/R_0$ of four Si-NR–based sensors between normal conditions and MI states, corresponding to each direction. Error bars correspond to the calculated SEM from six measurements.

sensors, such an OSG device package can simultaneously measure complex cardiac disorders that arise from variable directions/locations, such as possible occlusions in different vessels, at a one-time measurement within rapid duration.

Although OSG devices provide powerful capabilities for precise, rapid characterization of tissue biomechanics, a key feature is the need for wireless data transmission design. As a solution, we developed a wireless implantable/wearable platform design to allow continuous monitoring of tissue biomechanics. Here, fig. S25A presents the designed wireless platform of the OSG device that integrates the miniaturized microcontroller unit components and other modules such as power management. The microcontroller unit integrated with Bluetooth low energy function (NRF52832) can enable data recording and wireless transmission for direct delivery and simultaneous conversion to a portable device (i.e., a smartphone), through a customized application to achieve monitoring of mechanophysiological signals. The overall system can be fabricated on a flexible printed circuit board (2 cm by 3 cm, ~100 μm thick), serving as the basis for a biointegrated platform. Figure S25B demonstrates the real-time output of the OSG device under periodic strain cycles with intensity from 0 to 10%, in a wireless manner. Figure S25C illustrates the functional diagram of the wireless sensor system. Ongoing efforts focus on the realization of this design with multiplexed high-count channels with battery-free alternatives (*70*).

DISCUSSION

In summary, we introduce an OSG sensor using ultrathin monocrystalline Si-NRs for precise dynamic strain detection across a wide range with exceptional stability, serving as a wearable and implantable platform for mechanophysiological monitoring in a biocompatible fashion. The octopus-like Si-NRs exhibit direction-specific responses to strain. In vitro tests show a 1° relative deviation for strain direction and 0.1% of sensitivity as minimum strain detection. We demonstrate that high sensitivity to strain enables the sensor to real-time monitor mechanophysiological signals (e.g., IOP fluctuations and pulses). For example, in vivo trials on rat models confirm its efficacy in detecting cardiac abnormalities and accurately locating the pathological orientation. Integration of DCPU allows the device to fully degrade within the body in a biocompatible manner. This research offers possibilities of clinical significance for continuous monitoring of complex tissue surface biomechanics.

MATERIALS AND METHODS

Preparation of monocrystalline silicon–based strain sensor

The transfer printing process started with Radio Corporation of America cleaning of SOI wafer (500-nm Si/1-μm SiO_2; SOITEC). Boron doping of the cleaned wafer in a tube furnace (960°C for 15 min; N_2, 1 liter/min) obtained a final boron concentration of ~10^{20} atoms/cm^3. Dipping the doped wafer in buffered oxide etchant (BOE) removed the surface oxide layer formed in the doping process. Then, spin-coating photoresist S1805 (~1 μm; Dow) on the SOI wafer, followed by photolithography (MA6, SUSS) and reactive ion etching (RIE) (T2, Trion), created microholes (4-μm diameter/40-μm pitch) in the Si layer. Buried oxide layer etching in hydrogen fluoride (HF) solution (42%) for ~30 min released the top Si layer. Picking up the Si layer by a PDMS stamp (base, curing agent = 4:1) and pressing the stamp onto the receiver substrate transferred the Si layer from the SOI to the PI layer. Cleaning with acetone removed the S1805 and yielded the Si layer on a PI substrate.

Fabrication of the OSG device for omnidirectional sensing

Spin-coated polymethyl methacrylate (PMMA) (950 PMMA A7, ~1 μm; Microchem) and PI (~1.5 μm; Changzhou Ya'an New Material Co. Ltd.) on a cleaned glass wafer (3 cm by 3 cm) served as sacrificial layer and substrate layer, respectively. Curing of the PI substrate after transfer printing of top Si layer occurred at 210°C for 120 min. Photolithography and RIE etching defined Si-NR–based strain gauge with an octopus-like pattern. Magnetron sputtering of Cr/Au (10/200 nm; DE500, DE Technology) followed by lithographically patterning and wet etching defined the serpentine metal interconnects. Another coating of PI (~1.5 μm) served as encapsulation. Then, lithographically patterned exposure to RIE of the PI layers formed the mesh structure of the entire device for improved stretchability and robustness. Subsequently, immersing the sample in acetone (~13 hours) dissolved the sacrificial PMMA layer and released the device from glass wafer. Peeling the device from the glass substrate with a WST (3 M 5414 transparent) completed the fabrication process. For the OSG devices integrated with reusable PDMS substrates, the fabrication process starts with deposition of adhesive layers (Ti/SiO_2, 5/50 nm thick) on the backside of OSG devices, followed by transfer printing onto the PDMS substrate (30 μm thick; moduli of 500 kPa) via ultraviolet ozone treatment. In this manner, the OSG devices can intimately mount on tissues of interest via the soft elastomer. Conformal contact occurs via lamination in a simple, reversible manner that enables multiple times of use (100×).

Characterization and calibration of the Si-NR–based OSG devices

Programmable uniaxial motorized stage (DYCH-57H56SS, Dongyuan Chuanghui) provided applied strain ($\varepsilon_{appl.}$) by fixing the OSG device on the stage. The strain intensity was changed by adjusting the traveling distance of the motorized stage. The direction angle (φ) was changed through variation in angle of placement of the OSG device. Electrochemical workstation (CHI660e, CH Instruments Inc.) provided voltage supply and measured the real-time currents of Si-NR–based sensor to obtain the resistance data. The GF of the Si-NR–based sensor, taking the S1 sensor as an example, was calculated on the basis of the $\Delta R/R_0$ under applied strain ($\varepsilon_{appl.}$ = 10% and φ = 22.5°).

FEA simulation

The FEA commercial software Abaqus (Analysis User's Manual 2016) was used to validate the scientific accuracy of the shapes, to assess the credibility of the experimental results, and to evaluate the robustness of the devices. The device layers, including Au, Cr, Si, PI, and PDMS, were modeled by the four-node shell element S4R, with the minimal element size of 0.01 mm to ensure the convergence and the accuracy of the simulation results. The Si and PI are elastic materials, the Au and Cr are elastoplastic materials, and the PDMS is a Neo-Hooke model–based hyperelastic material. The material properties are as follows: E_{Au} = 70 GPa, ν_{Au} = 0.44, $\sigma_{s,\,Au}$ = 200 MPa, E_{Cr} = 279 GPa, ν_{Cr} = 0.21, $\sigma_{s,\,Cr}$ = 500 MPa, E_{Si} = 166 GPa, ν_{Si} = 0.27, E_{PI} = 1 GPa, ν_{PI} = 0.34, $D_{1,PDMS} = \frac{6(1-2\nu_{PDMS})}{E_{PDMS}}$ = 0.24 MPa^{-1}, and

$C_{10,\mathrm{PDMS}} = \frac{E_{\mathrm{PDMS}}}{4(1+\nu_{\mathrm{PDMS}})} = 0.084$ MPa, where E represents Young's modulus, ν represents Poisson ratio, σ_s represents yield stress, C_{10} represents shear modulus, and D_1 represents bulk modulus. The stretching, bending, and twisting tests were implemented by the "Static, General" analysis step throughout this study.

Synthesis of b-DCPU for encapsulating the bioelectronics

The preparation involved dissolving and mixing hexamethylene diisocyanate and melted polycaprolactone triol in butyl acetate at 60°C and adding tin(II) 2-ethylhexanoate as the catalyst. Drop-casting the mixture onto the surface of doped silicon wafers followed by baking at 60°C for 24 hours formed translucent polymer films. Using the capillary-assisted electrochemical delamination method detached the film from silicon wafer and yielded free-standing b-DCPU (*51*).

Fabrication of biodegradable implantable devices

The process began with spin-coating and curing of PDMS (base, curing agent = 10:1) on a clean glass wafer. Lamination of a Kapton film (~5 μm; DuPont) on the cured PDMS served as the transfer printing substrate. The subsequent device preparation process resembled the one described previously, except for changing the metal interconnect from Au to Mo. The transfer involved peeling off the Kapton film, along with the device, from the glass substrate and then inversely mounting it onto a layer of DCPU (~50 μm) synthesized on a silicon wafer. Elimination of the top PI layer by RIE, followed by lamination of another DCPU layer (~50 μm) on the device, served as encapsulation. Using the capillary-assisted electrochemical delamination method detached the transient device from the substrate.

Cytotoxicity evaluation

The Si-NR–based strain gauge was sterilized by ultraviolet irradiation and cocultured with L929 cells (Procell Life Science & Technology Co. Ltd.) for 24, 48, and 72 hours, respectively, in a constant temperature incubator (37°C). The cultured cells were stained by calcein acetoxymethyl/propidium iodide (AM/PI) double-stain kit (BB-4126, BestBio) and incubated for 15 min at room temperature. Fluorescence microscope was used to obtain the images of dyed live and dead cells. To evaluate the relative cell viability, the cocultured cells were added to culture medium containing 10% CCK-8 (IV08-100, Invigentech) and incubated for 2 hours at 37°C. The absorbance value at 450 nm detected by microplate reader was used to reflect the relative viability of cells.

Wearable applications in mechanophysiological monitoring

All participants for the study were fully voluntary and submitted the informed consent before experiments and approved by the Ethics Committee of Tongji Hospital Affiliated to Tongji University (approved number: 2022-113). For detection of facial expression, the OSG device was located nearby the angulus oris of a volunteer human individual, with S2 sensor aligned to the vertical axis of the face, via a bioglue (Derma-tac, Smooth-On Inc.). To monitor the pulse signals, the OSG device was laminated on the neck and the wrist of a volunteer human individual, respectively, both at the positions with the largest deformation. To evaluate the influence of translational or vibrational motion on mechanophysiological signal monitoring, the OSG device was laminated on the neck and finger joint of volunteer human individual, respectively, to detect carotid pulse signals and finger bending motion signals before and after motion (running and cycling). To representatively assess the stable performance of OSG device under different conditions, the OSG device was placed at the back of the neck to monitor head motion on the dry and sweaty skin, respectively. Porcine eyeballs came from a regular slaughterhouse within 4 hours. In the case of IOP monitoring, the test platform was demonstrated in Fig. 4B, where the fluctuation of IOP was realized by the regulation of volume of fluid pumped in and out the anterior chamber through a tube controlled by microinjection pump (Harvard Apparatus). The OSG device was mounted on the center of the eyeball, and the IOP inside was calibrated by a commercial pressure sensor (Testo 510i). In all cases, the working voltage was set as 1 V. Each of the experiments was performed at least three times.

In vivo experiment of animal models

All the animal experiments have been approved by the Ethics Committee of Shanghai Shengchang Biotechnology Co. Ltd. (approved number: 2023-09-FDDX-SEM-082) and conducted under its supervision. All in vivo experiments were performed on 6-week-old Sprague-Dawley male rats. After making an oblique skin incision with a scalpel, the ribs were exposed by blunt dissection of the subcutaneous tissue. The third intercostal space was identified, and an incision of approximately 6 to 8 mm was made. The thoracic cavity is then opened by blunt dissection of the tissue in the intercostal space. The Si-NR–based strain gauge was mounted on different regions of the heart via bioglue (Compont) to achieve conformal attachment to the epicardium. The hypoxia model was constructed by removing the respiratory intubation for oxygen supply after open-heart surgery. The MI model was constructed by ligation of the LAD vessel in rats. The anterior wall of the LV turned white after ligation, confirming the cessation of LAD blood flow.

Supplementary Materials

The PDF file includes:

Texts S1 to S6
Figs. S1 to S25
Tables S1 and S2
Legend for movie S1

Other Supplementary Material for this manuscript includes the following:

Movie S1

REFERENCES AND NOTES

1. S.-H. Sunwoo, S. I. Han, C. S. Park, J. H. Kim, J. S. Georgiou, S.-P. Lee, D.-H. Kim, T. Hyeon, Soft bioelectronics for the management of cardiovascular diseases. *Nat. Rev. Bioeng.* **2**, 8–24 (2024).
2. G. Y. Lee, C. T. Lim, Biomechanics approaches to studying human diseases. *Trends Biotechnol.* **25**, 111–118 (2007).
3. E. Song, Y. Huang, N. Huang, Y. Mei, X. Yu, J. A. Rogers, Recent advances in microsystem approaches for mechanical characterization of soft biological tissues. *Microsyst. Nanoeng.* **8**, 77 (2022).
4. M. Lin, H. Hu, S. Zhou, S. Xu, Soft wearable devices for deep-tissue sensing. *Nat. Rev. Mater.* **7**, 850–869 (2022).
5. H. Arioz Habibi, E. Alici Davutoglu, S. G. Kandemirli, M. Aslan, A. Ozel, A. Kalyoncu Ucar, P. Zeytun, R. Madazli, I. Adaletli, In vivo assessment of placental elasticity in intrauterine growth restriction by shear-wave elastography. *Eur. J. Radiol.* **97**, 16–20 (2017).
6. H. Kim, B. Rigo, G. Wong, Y. J. Lee, W. H. Yeo, Advances in wireless, batteryless, implantable electronics for real-time, continuous physiological monitoring. *Nanomicro Lett.* **16**, 52 (2023).
7. W. Gao, C. Yu, Wearable and implantable devices for healthcare. *Adv. Healthc. Mater.* **10**, 2101548 (2021).

8. S. M. A. Iqbal, I. Mahgoub, E. Du, M. A. Leavitt, W. Asghar, Advances in healthcare wearable devices. *Npj Flex. Electron.* **5**, 9 (2021).
9. S.-H. Sunwoo, S. I. Han, D. Jung, M. Kim, S. Nam, H. Lee, S. Choi, H. Kang, Y. S. Cho, D.-H. Yeom, M.-J. Cha, S. Lee, S.-P. Lee, T. Hyeon, D.-H. Kim, Stretchable low-impedance conductor with Ag–Au–Pt core–shell–shell nanowires and in situ formed Pt nanoparticles for wearable and implantable device. *ACS Nano* **17**, 7550–7561 (2023).
10. J. Grune, M. Yamazoe, M. Nahrendorf, Electroimmunology and cardiac arrhythmia. *Nat. Rev. Cardiol.* **18**, 547–564 (2021).
11. F. Migliore, G. Mattesi, A. Zorzi, B. Bauce, I. Rigato, D. Corrado, A. Cipriani, Arrhythmogenic cardiomyopathy–current treatment and future options. *J. Clin. Med.* **10**, 2750 (2021).
12. T. Sun, F. Tasnim, R. T. McIntosh, N. Amiri, D. Solav, M. T. Anbarani, D. Sadat, L. Zhang, Y. Gu, M. A. Karami, C. Dagdeviren, Decoding of facial strains via conformable piezoelectric interfaces. *Nat. Biomed. Eng.* **4**, 954–972 (2020).
13. C. Yang, X. Huang, X. Li, C. Yang, T. Zhang, Q. Wu, D. Liu, H. Lin, W. Chen, N. Hu, X. Xie, Wearable and implantable intraocular pressure biosensors: Recent progress and future prospects. *Adv. Sci.* **8**, 2002971 (2021).
14. S. Ji, C. Wan, T. Wang, Q. Li, G. Chen, J. Wang, Z. Liu, H. Yang, X. Liu, X. Chen, Water-resistant conformal hybrid electrodes for aquatic endurable electrocardiographic monitoring. *Adv. Mater.* **32**, 2001496 (2020).
15. Z. Lou, J. Tao, B. Wei, X. Jiang, S. Cheng, Z. Wang, C. Qin, R. Liang, H. Guo, L. Zhu, P. Muller-Buschbaum, H.-M. Cheng, X. Xu, Near-infrared organic photodetectors toward skin-integrated photoplethysmography-electrocardiography multimodal sensing system. *Adv. Sci.* **10**, 2304174 (2023).
16. S. Yang, J. Cheng, J. Shang, C. Hang, J. Qi, L. Zhong, Q. Rao, L. He, C. Liu, L. Ding, M. Zhang, S. Chakrabarty, X. Jiang, Stretchable surface electromyography electrode array patch for tendon location and muscle injury prevention. *Nat. Commun.* **14**, 6494 (2023).
17. C. Wang, H. Wang, B. Wang, H. Miyata, Y. Wang, M. O. G. Nayeem, J. J. Kim, S. Lee, T. Yokota, H. Onodera, T. Someya, On-skin paintable biogel for long-term high-fidelity electroencephalogram recording. *Sci. Adv.* **8**, eabo1396 (2022).
18. T. Kim, Y. Shin, K. Kang, K. Kim, G. Kim, Y. Byeon, H. Kim, Y. Gao, J. R. Lee, G. Son, T. Kim, Y. Jun, J. Kim, J. Lee, S. Um, Y. Kwon, B. G. Son, M. Cho, M. Sang, J. Shin, K. Kim, J. Suh, H. Choi, S. Hong, H. Cheng, H. G. Kang, D. Hwang, K. J. Yu, Ultrathin crystalline-silicon-based strain gauges with deep learning algorithms for silent speech interfaces. *Nat. Commun.* **13**, 5815 (2022).
19. X. Yu, H. Wang, X. Ning, R. Sun, H. Albadawi, M. Salomao, A. C. Silva, Y. Yu, L. Tian, A. Koh, C. M. Lee, A. Chempakasseril, P. Tian, M. Pharr, J. Yuan, Y. Huang, R. Oklu, J. A. Rogers, Needle-shaped ultrathin piezoelectric microsystem for guided tissue targeting via mechanical sensing. *Nat. Biomed. Eng.* **2**, 165–172 (2018).
20. C. Dagdeviren, Y. Shi, P. Joe, R. Ghaffari, G. Balooch, K. Usgaonkar, O. Gur, P. L. Tran, J. R. Crosby, M. Meyer, Y. Su, R. Chad Webb, A. S. Tedesco, M. J. Slepian, Y. Huang, J. A. Rogers, Conformal piezoelectric systems for clinical and experimental characterization of soft tissue biomechanics. *Nat. Mater.* **14**, 728–736 (2015).
21. J. Lyu, Q. Zhou, H. Wang, Q. Xiao, Z. Qiang, X. Li, J. Wen, C. Ye, M. Zhu, Mechanically strong, freeze-resistant, and ionically conductive organohydrogels for flexible strain sensors and batteries. *Adv. Sci.* **10**, 2206591 (2023).
22. S. Lee, S. Franklin, F. A. Hassani, T. Yokota, M. O. G. Nayeem, Y. Wang, R. Leib, G. Cheng, D. W. Franklin, T. Someya, Nanomesh pressure sensor for monitoring finger manipulation without sensory interference. *Science* **370**, 966–970 (2020).
23. H. Chen, F. Zhuo, J. Zhou, Y. Liu, J. Zhang, S. Dong, X. Liu, A. Elmarakbi, H. Duan, Y. Fu, Advances in graphene-based flexible and wearable strain sensors. *Chem. Eng. J.* **464**, 142576 (2023).
24. Z. Liu, X. Hu, R. Bo, Y. Yang, X. Cheng, W. Pang, Q. Liu, Y. Wang, S. Wang, S. Xu, Z. Shen, Y. Zhang, A three-dimensionally architected electronic skin mimicking human mechanosensation. *Science* **384**, 987–994 (2024).
25. S. Yang, N. Lu, Gauge factor and stretchability of silicon-on-polymer strain gauges. *Sensors* **13**, 8577–8594 (2013).
26. Z. Jiang, N. Chen, Z. Yi, J. Zhong, F. Zhang, S. Ji, R. Liao, Y. Wang, H. Li, Z. Liu, Y. Wang, T. Yokota, X. Liu, K. Fukuda, X. Chen, T. Someya, A 1.3-micrometre-thick elastic conductor for seamless on-skin and implantable sensors. *Nat. Electron.* **5**, 784–793 (2022).
27. Z. Zhang, J. Yang, H. Wang, C. Wang, Y. Gu, Y. Xu, S. Lee, T. Yokota, H. Haick, T. Someya, Y. Wang, A 10-micrometer-thick nanomesh-reinforced gas-permeable hydrogel skin sensor for long-term electrophysiological monitoring. *Sci. Adv.* **10**, eadj5389 (2024).
28. R. C. Webb, A. P. Bonifas, A. Behnaz, Y. Zhang, K. J. Yu, H. Cheng, M. Shi, Z. Bian, Z. Liu, Y.-S. Kim, W.-H. Yeo, J. S. Park, J. Song, Y. Li, Y. Huang, A. M. Gorbach, J. A. Rogers, Ultrathin conformal devices for precise and continuous thermal characterization of human skin. *Nat. Mater.* **12**, 938–944 (2013).
29. Z. Sui, I. P. Herman, Effect of strain on phonons in Si, Ge, and Si/Ge heterostructures. *Phys. Rev. B.* **48**, 17938–17953 (1993).
30. C.-Y. Peng, C.-F. Huang, Y.-C. Fu, Y.-H. Yang, C.-Y. Lai, S.-T. Chang, C. W. Liu, Comprehensive study of the Raman shifts of strained silicon and germanium. *J. Appl. Phys.* **105**, 083537 (2009).
31. N. S. Lu, X. Wang, Z. G. Suo, J. Vlassak, Metal films on polymer substrates stretched beyond 50%. *Appl. Phys. Lett.* **91**, 221909 (2007).
32. Z.-Q. Gao, C.-H. Liu, S.-L. Zhang, S.-H. Li, L.-W. Gao, R.-L. Chai, T.-Y. Zhou, X.-J. Ma, X. Li, S. Li, J. Zhao, Q. Zhao, Lanternarene-based self-sorting double-network hydrogels for flexible strain sensors. *Small* , 2404231 (2024).
33. C. M. Boutry, Y. Kaizawa, B. C. Schroeder, A. Chortos, A. Legrand, Z. Wang, J. Chang, P. Fox, Z. Bao, A stretchable and biodegradable strain and pressure sensor for orthopaedic application. *Nat. Electron.* **1**, 314–321 (2018).
34. L. Zhang, S. Xing, H. Yin, H. Weisbecker, H. T. Tran, Z. Guo, T. Han, Y. Wang, Y. Liu, Y. Wu, W. Xie, C. Huang, W. Luo, M. Demaesschalck, C. McKinney, S. Hankley, A. Huang, B. Brusseau, J. Messenger, Y. Zou, W. Bai, Skin-inspired, sensory robots for electronic implants. *Nat. Commun.* **15**, 4777 (2024).
35. J. H. Lee, S. H. Kim, J. S. Heo, J. Y. Kwak, C. W. Park, I. Kim, M. Lee, H. H. Park, Y. H. Kim, S. J. Lee, S. K. Park, Heterogeneous structure omnidirectional strain sensor arrays with cognitively learned neural networks. *Adv. Mater.* **35**, 2208184 (2023).
36. Z. Luo, X. Li, Q. Li, X. Tian, T. Fan, C. Wang, X. Wu, G. Shen, In situ dynamic manipulation of graphene strain sensor with drastically sensing performance enhancement. *Adv. Electron. Mater.* **6**, 2000269 (2020).
37. X. Shi, H. Wang, X. Xie, Q. Xue, J. Zhang, S. Kang, C. Wang, J. Liang, Y. Chen, Bioinspired ultrasensitive and stretchable MXene-based strain sensor via nacre-mimetic microscale "brick-and-mortar" architecture. *ACS Nano* **13**, 649–659 (2019).
38. L. Xu, S. R. Gutbrod, A. P. Bonifas, Y. Su, M. S. Sulkin, N. Lu, H.-J. Chung, K.-I. Jang, Z. Liu, M. Ying, C. Lu, R. C. Webb, J.-S. Kim, J. I. Laughner, H. Cheng, Y. Liu, A. Ameen, J.-W. Jeong, G.-T. Kim, Y. Huang, I. R. Efimov, J. A. Rogers, 3D multifunctional integumentary membranes for spatiotemporal cardiac measurements and stimulation across the entire epicardium. *Nat. Commun.* **5**, 3329 (2014).
39. D. Son, J. Lee, S. Qiao, R. Ghaffari, J. Kim, J. E. Lee, C. Song, S. J. Kim, D. J. Lee, S. W. Jun, S. Yang, M. Park, J. Shin, K. Do, M. Lee, K. Kang, C. S. Hwang, N. Lu, T. Hyeon, D.-H. Kim, Multifunctional wearable devices for diagnosis and therapy of movement disorders. *Nat. Nanotechnol.* **9**, 397–404 (2014).
40. D.-H. Kim, R. Ghaffari, N. Lu, S. Wang, S. P. Lee, H. Keum, R. D'Angelo, L. Klinker, Y. Su, C. Lu, Y.-S. Kim, A. Ameen, Y. Li, Y. Zhang, B. de Graff, Y.-Y. Hsu, Z. Liu, J. Ruskin, L. Xu, C. Lu, F. G. Omenetto, Y. Huang, M. Mansour, M. J. Slepian, J. A. Rogers, Electronic sensor and actuator webs for large-area complex geometry cardiac mapping and therapy. *Proc. Natl. Acad. Sci. U.S.A.* **109**, 19910–19915 (2012).
41. G. Singh, A. Chanda, Mechanical properties of whole-body soft human tissues: A review. *Biomed. Mater.* **16**, 062004 (2021).
42. G. N. Greaves, A. L. Greer, R. S. Lakes, T. Rouxel, Poisson's ratio and modern materials. *Nat. Mater.* **10**, 823–837 (2011).
43. G. Yang, X. Tang, G. Zhao, Y. Li, C. Ma, X. Zhuang, J. Yan, Highly sensitive, direction-aware, and transparent strain sensor based on oriented electrospun nanofibers for wearable electronic applications. *Chem. Eng. J.* **435**, 135004 (2022).
44. C. You, H. Zhao, Q. Guo, Y. Mei, Material strategies for on-demand smart transient electronics. *MRS Bull.* **45**, 129–134 (2020).
45. Y. Choi, J. Koo, J. A. Rogers, Inorganic materials for transient electronics in biomedical applications. *MRS Bull.* **45**, 103–112 (2020).
46. Y. K. Lee, K. J. Yu, E. Song, A. Barati Farimani, F. Vitale, Z. Xie, Y. Yoon, Y. Kim, A. Richardson, H. Luan, Y. Wu, X. Xie, T. H. Lucas, K. Crawford, Y. Mei, X. Feng, Y. Huang, B. Litt, N. R. Aluru, L. Yin, J. A. Rogers, Dissolution of monocrystalline silicon nanomembranes and their use as encapsulation layers and electrical interfaces in water-soluble electronics. *ACS Nano* **11**, 12562–12572 (2017).
47. C. Fernandes, I. Taurino, Biodegradable molybdenum (Mo) and tungsten (W) devices: One step closer towards fully-transient biomedical implants. *Sensors* **22**, 3062 (2022).
48. Y. S. Choi, Y.-Y. Hsueh, J. Koo, Q. Yang, R. Avila, B. Hu, Z. Xie, G. Lee, Z. Ning, C. Liu, Y. Xu, Y. J. Lee, W. Zhao, J. Fang, Y. Deng, S. M. Lee, A. Vázquez-Guardado, I. Stepien, Y. Yan, J. W. Song, C. Haney, Y. S. Oh, W. Liu, H.-J. Yoon, A. Banks, M. R. MacEwan, G. A. Ameer, W. Z. Ray, Y. Huang, T. Xie, C. K. Franz, S. Li, J. A. Rogers, Stretchable, dynamic covalent polymers for soft, long-lived bioresorbable electronic stimulators designed to facilitate neuromuscular regeneration. *Nat. Commun.* **11**, 5990 (2020).
49. S. Chen, Z. Wu, C. Chu, Y. Ni, R. E. Neisiany, Z. You, Biodegradable elastomers and gels for elastic electronics. *Adv. Sci.* **9**, 2105146 (2022).
50. S.-W. Hwang, G. Park, C. Edwards, E. A. Corbin, S.-K. Kang, H. Cheng, J.-K. Song, J.-H. Kim, S. Yu, J. Ng, J. E. Lee, J. Kim, C. Yee, B. Bhaduri, Y. Su, F. G. Omennetto, Y. Huang, R. Bashir, L. Goddard, G. Popescu, K.-M. Lee, J. A. Rogers, Dissolution chemistry and biocompatibility of single-crystalline silicon nanomembranes and associated materials for transient electronics. *ACS Nano* **8**, 5843–5851 (2014).
51. J. Yin, S. Wang, T. Tat, J. Chen, Motion artefact management for soft bioelectronics. *Nat. Rev. Bioeng.* **2**, 541–558 (2024).
52. N. Rodeheaver, R. Herbert, Y.-S. Kim, M. Mahmood, H. Kim, J.-W. Jeong, W.-H. Yeo, Strain-isolating materials and interfacial physics for soft wearable bioelectronics and wireless, motion artifact-controlled health monitoring. *Adv. Funct. Mater.* **31**, 2104070 (2021).
53. A. H. Chowdhury, B. Jafarizadeh, A. R. Baboukani, N. Pala, C. Wang, Monitoring and analysis of cardiovascular pulse waveforms using flexible capacitive and piezoresistive pressure sensors and machine learning perspective. *Biosens. Bioelectron.* **237**, 115449 (2023).

54. J. Li, H. Jia, J. Zhou, X. Huang, L. Xu, S. Jia, Z. Gao, K. Yao, D. Li, B. Zhang, Y. Liu, Y. Huang, Y. Hu, G. Zhao, Z. Xu, J. Li, C. K. Yiu, Y. Gao, M. Wu, Y. Jiao, Q. Zhang, X. Tai, R. H. Chan, Y. Zhang, X. Ma, X. Yu, Thin, soft, wearable system for continuous wireless monitoring of artery blood pressure. *Nat. Commun.* **14**, 5009 (2023).
55. T. Tamura, Y. Maeda, M. Sekine, M. Yoshida, Wearable photoplethysmographic sensor-past and present. *Electronics* **3**, 282–302 (2014).
56. C. Wang, X. Li, H. Hu, L. Zhang, Z. Huang, M. Lin, Z. Zhang, Z. Yin, B. Huang, H. Gong, S. Bhaskaran, Y. Gu, M. Makihata, Y. Guo, Y. Lei, Y. Chen, C. Wang, Y. Li, T. Zhang, Z. Chen, A. P. Pisano, L. Zhang, Q. Zhou, S. Xu, Monitoring of the central blood pressure waveform via a conformal ultrasonic device. *Nat. Biomed. Eng.* **2**, 687–695 (2018).
57. Y. Fu, S. Zhao, L. Wang, R. Zhu, A wearable sensor using structured silver-particle reinforced PDMS for radial arterial pulse wave monitoring. *Adv. Healthc. Mater.* **8**, 1900633 (2019).
58. S. Li, H. Wang, W. Ma, L. Qiu, K. Xia, Y. Zhang, H. Lu, M. Zhu, X. Liang, X. E. Wu, H. Liang, Y. Zhang, Monitoring blood pressure and cardiac function without positioning via a deep learning-assisted strain sensor array. *Sci. Adv.* **9**, eadh0615 (2023).
59. W. W. Nichols, Clinical measurement of arterial stiffness obtained from noninvasive pressure waveforms. *Am. J. Hypertens.* **18**, 3S–10S (2005).
60. J. Park, M. Kim, Y. Lee, H. S. Lee, H. Ko, Fingertip skin-inspired microstructured ferroelectric skins discriminate static/dynamic pressure and temperature stimuli. *Sci. Adv.* **1**, e1500661 (2015).
61. S. Wang, Y. Fang, H. He, L. Zhang, C. A. Li, J. Ouyang, Wearable stretchable dry and self-adhesive strain sensors with conformal contact to skin for high-quality motion monitoring. *Adv. Funct. Mater.* **31**, 2007495 (2021).
62. M. Wang, Z. Yan, T. Wang, P. Cai, S. Gao, Y. Zeng, C. Wan, H. Wang, L. Pan, J. Yu, S. Pan, K. He, J. Lu, X. Chen, Gesture recognition using a bioinspired learning architecture that integrates visual data with somatosensory data from stretchable sensors. *Nat. Electron.* **3**, 563–570 (2020).
63. S.-H. Sunwoo, M.-J. Cha, S. I. Han, H. Kang, Y. S. Cho, D.-H. Yeom, C. S. Park, N. K. Park, S. W. Choi, S. J. Kim, G. D. Cha, D. Jung, S. Choi, S. Oh, G.-B. Nam, T. Hyeon, D.-H. Kim, S.-P. Lee, Ventricular tachyarrhythmia treatment and prevention by subthreshold stimulation with stretchable epicardial multichannel electrode array. *Sci. Adv.* **9**, eadf6856 (2023).
64. C. M. Albert, W. G. Stevenson, The future of arrhythmias and electrophysiology. *Circulation* **133**, 2687–2696 (2016).
65. R. J. Julian, The response of the heart and pulmonary arteries to hypoxia, pressure, and volume. A short review. *Poult. Sci.* **86**, 1006–1011 (2007).
66. N. Si, K. Shi, N. Li, X. Dong, C. Zhu, Y. Guo, J. Hu, J. Cui, F. Yang, T. Zhang, Identification of patients with acute myocardial infarction based on coronary CT angiography: The value of pericoronary adipose tissue radiomics. *Eur. Radiol.* **32**, 6868–6877 (2022).
67. P. S. Rajendran, K. Nakamura, O. A. Ajijola, M. Vaseghi, J. A. Armour, J. L. Ardell, K. Shivkumar, Myocardial infarction induces structural and functional remodelling of the intrinsic cardiac nervous system. *J. Physiol.* **594**, 321–341 (2016).
68. N. G. Frangogiannis, The inflammatory response in myocardial injury, repair, and remodelling. *Nat. Rev. Cardiol.* **11**, 255–265 (2014).
69. A. Ushakov, V. Ivanchenko, A. Gagarina, Regulation of myocardial extracellular matrix dynamic changes in myocardial infarction and postinfarct remodeling. *Curr. Cardiol. Rev.* **16**, 11–24 (2020).
70. P. Gutruf, R. T. Yin, K. B. Lee, J. Ausra, J. A. Brennan, Y. Qiao, Z. Xie, R. Peralta, O. Talarico, A. Murillo, S. W. Chen, J. P. Leshock, C. R. Haney, E. A. Waters, C. Zhang, H. Luan, Y. Huang, G. Trachiotis, I. R. Efimov, J. A. Rogers, Wireless, battery-free, fully implantable multimodal and multisite pacemakers for applications in small animal models. *Nat. Commun.* **10**, 5742 (2019).

Acknowledgments: Part of the experimental work was carried out in Fudan Nanofabrication Laboratory. **Funding:** This work is supported by the STI 2030-Major Project (2022ZD0209900), the National Natural Science Foundation of China (62204057, 62304044, and 12022209), Science and Technology Commission of Shanghai Municipality (22ZR1406400), and Lingang Laboratory (LG-QS-202202-02). We appreciate the support by Shanghai Municipal Science and Technology Major Project (2018SHZDZX01), ZJ laboratory, Shanghai Center for Brain Science and Brain-Inspired Technology, the young scientist project of MOE innovation platform, and the China Postdoctoral Science Foundation (2023 M730712). **Author contributions:** B.H. and E.S. designed the study. D.X., J. Li, B.W., and R.L. performed the structural designs and theoretical analysis. B.H., Y.S., and P.W. prepared the tissue samples and in vivo experiments. Z.N. and M.H. fabricated the biodegradable device. P.L., L.Z., N.H., J. Liu, Y.L., Z.W., and Y.M. assisted in the device fabrication and experimental investigations. B.H., D.X., Y.S., and Z.N. wrote the draft. B.H., D.X., R.L., M.H., and E.S. reviewed and edited the manuscript. **Competing interests:** The authors declare that they have no competing interests. **Data and materials availability:** All data needed to evaluate the conclusions in the paper are present in the paper and/or the Supplementary Materials.

Submitted 16 April 2024
Accepted 5 September 2024
Published 9 October 2024
10.1126/sciadv.adp8804